Response to Editor Florent Domine's comment on "The mechanical origin of snow avalanche dynamics and flow regime transitions"

Xingyue Li, Betty Sovilla, Chenfanfu Jiang, and Johan Gaume*
*Correspondence: johan.gaume@epfl.ch
August 4th, 2020

We thank the editor for his positive evaluation of our responses and his suggestion on the manuscript. Our detailed reply is provided below. The point-to-point responses to the reviewers' comments have been attached as we have added line numbers to locate our answers. In addition, a marked-up manuscript with tracked changes is attached.

Editor:

Thank you for your detailed and adequate responses to the Reviewers' comments. Please upload your revised version. Please also be careful to read our instructions regarding the difference between supplementary material and appendices.

https://www.the-cryosphere.net/for_authors/manuscript_preparation.html

It is likely that what you plan to add as supplementary material in your response to Reviewer 1 should in fact be included as an appendix.

I look forward to reading your revised version.

Reply: We have added the planned supplement about energy evolution as an appendix in the revised manuscript (Pages 24-26). Correspondingly, we have cited the appendix in Lines 156-157 in the revision.

Response to Reviewer #1 Frederic Dufour's comment

We want to thank Prof. Dufour for his comments and his constructive suggestions that helped us to improve the quality of our paper. In the following, we provide detailed point-by-point answers to the comments raised by the reviewer.

The paper by X. Li, B. Sovilla, C. Jiang and J. Gaume entitled The mechanical origin of snow avalanche dynamics and flow regime transitions is well organised and written with a short introduction, three sections presenting the different steps of the work and some conclusions and perspectives to finish with.

Reply: We thank the reviewer for this positive evaluation of our paper.

In the introduction, the applicative context is first depicted regarding the necessity of investigating the snow avalanche dynamics for a better understanding and protection of people and human goods. The originality of this study is justified by the need of having a numerical tool to model the dynamics of snow avalanches with snow of different types and different slope geometries.

In section 2, the MPM is briefly described, as well as the constitutive model mainly referring to former contributions by some of the authors but not solely.

Section 3 presents a complete parametric study of five snow types flowing along ideal slopes and arresting on a horizontal plane. The inclination and length of the slope are also part of the parametric study. All simulations fall into four typical snow avalanche groups denoted cold dense, warm shear, warm plug and sliding slab. The front velocity, the velocity profile across the flow, the arresting distance and the free surface shape are part of the output parameters analysed. The results are qualitatively in agreement with the physics and discussed as such. The influence of the snow type is systematically explained. Unfortunately, only macroscopic quantities (see above) as output are studied to distinguish flow types. I would suggest, as in Gracia et al. (2019) [F. Gracia, P. Villard, V. Richefeu (2019) Comparison of two numerical approaches (DEM and MPM) applied to unsteady flow, Computational Particle Mechanics, 6(4), pp. 591-609] which deals with the same topic applied to granular flows, in order to understand the internal physics of the flow that you extract, show and discuss some quantities such as energies (potential, kinetic, dissipated by friction or fracture) to understand their transfers during the flow and to provide an insight to understand which material parameters, including the basal friction coefficient, are the key ones. Some master curves or should I say master clouds are proposed with dimensionless parameters. Proposition of analytical solutions fitting the simulated results would be an interesting point for further uses towards a quantitative step.

Reply: The basis for analysing energy is energy conservation. The constitutive model adopted in this study perfectly satisfies the second law of thermodynamics (Line 119-120 in the marked-up manuscript). Following the derivation in Gaume et al. (2018),

proving that energy does not increase is equivalent to proving the plastic dissipation rate $\dot{w}^P(\boldsymbol{X}, t)$ is non-negative. $\dot{w}^P$ can be computed as

$$\dot{w}^P = -\boldsymbol{\tau} : \frac{1}{2}(\mathcal{L}_v \boldsymbol{b}^E)(\boldsymbol{b}^E)^{-1}$$

where $\boldsymbol{\tau}$ is the Kirchhoff stress tensor, $\mathcal{L}_v$ is the Lie derivative, and $\boldsymbol{b}^E$ is the elastic right Cauchy-Green strain tensor. Since we use an associative flow rule, $\mathcal{L}_v \boldsymbol{b}^E = -2\dot{\gamma}\frac{\partial y}{\partial \boldsymbol{\tau}}\boldsymbol{b}^E$ (see Equation 10 in Gaume et al. (2018)), $\dot{w}^P$ can be expressed as

$$\dot{w}^P = \boldsymbol{\tau} : \dot{\gamma}\frac{\partial y}{\partial \boldsymbol{\tau}} = \dot{\gamma}\hat{\boldsymbol{\tau}} \cdot \frac{\partial y}{\partial \hat{\boldsymbol{\tau}}}$$

Recall that $\dot{\gamma} \geq 0$ in Equation 11 in Gaume et al. (2018). Furthermore, $\hat{\boldsymbol{\tau}} \cdot \frac{\partial y}{\partial \hat{\boldsymbol{\tau}}} \geq 0$ because our yield surface is a convex function of $\hat{\boldsymbol{\tau}}$ which includes the origin. Therefore $\dot{w}^P \geq 0$. Note that this result holds for any isotropic plasticity model that has a convex yield function and an associative flow rule.
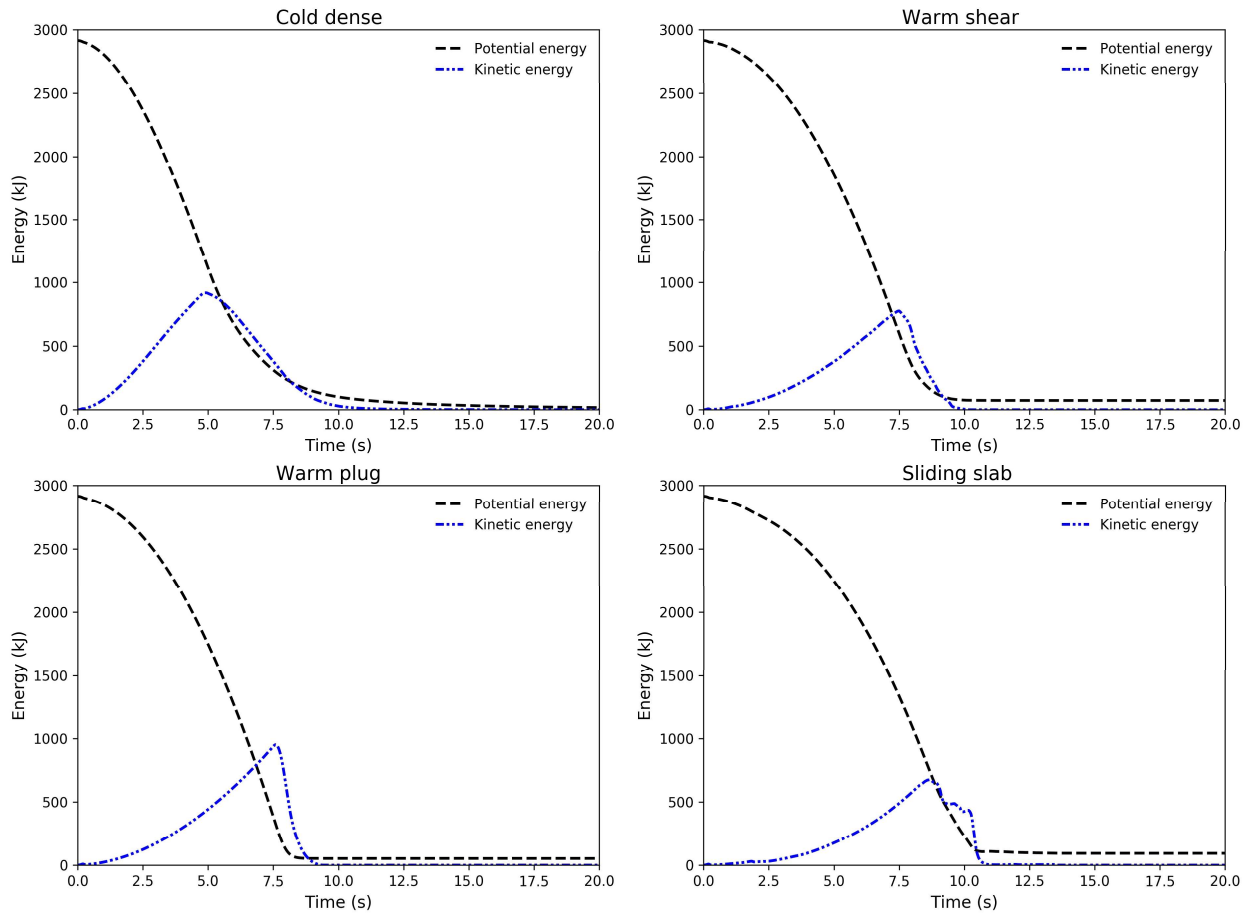

Figure 1. Evolution of potential and kinetic energy of the flows in the four typical flow regimes.

The evolution of kinetic and potential energy of the flows in the four typical flow regimes (i.e. cold dense, warm shear, warm plug, sliding slab) is shown in Fig. 1. As expected, the potential energy of the flows initially decreases as the flows move down from the slope, and then becomes steady after the flows stop. The kinetic energy of the flows

firstly increases and then reduces until it vanishes. It is noticed that the kinetic energy of the sliding slab shows fluctuations in the deceleration phase, due to the interactions between the separating slabs in the flow after they reach the connecting arc zone (see supplementary video 1).

Fig. 2 shows the dissipated energy of the flows in the four cases. The dissipated energy increases before it reaches the final steady state. The growth rate of the dissipated energy varies for the different flows as they have distinct flow behaviours. Nevertheless, the final energy dissipation does not show much difference for the different flows. This is because of the identical initial potential energy and the similar final potential energy of the flows.
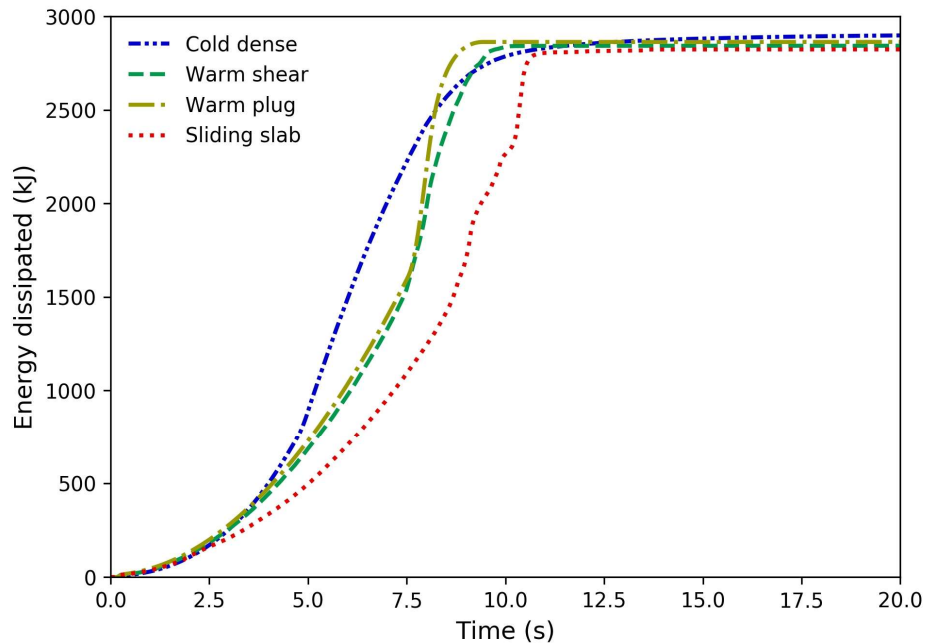

Figure 2. Evolution of dissipated energy of the flows in the four typical flow regimes.

The energy dissipation is contributed from 1) internal force of the material and 2) external force on the material from the boundary/slope. As illustrated in Fig. 3, in all the four cases, the dissipated energy from the boundary is much higher than that dissipated inside the material. This is consistent with the results in Gracia et al. (2019).

From the above discussion, we can indeed get more information about the energies. However, we did not find contrasting distinction characterizing the different flow regimes of the flows. Therefore, we put the above discussion as an appendix (Page 24-26) cited in Lines 156-157.

Regarding the analytical solutions fitting the simulated results, we indeed thought about proposing analytical relations between the scaled maximum velocity and the scaled deposit height in Fig. 7 in our manuscript as well as between the scaled maximum velocity and the scaled runout angle in Fig. 10. However, the physical processes involved are strongly non-linear and too complicated to develop analytical solutions. For

example, the deposit height and the runout distance are greatly affected by multiple processes during the flow and deposition, including breakage and granulation of snow, surging, and piling up. While we propose highly simplified analytical solutions based on the block sliding theory, as a limit case, the development of a complete analytical model taking into account all previously mentioned processes is beyond the scope of this study.
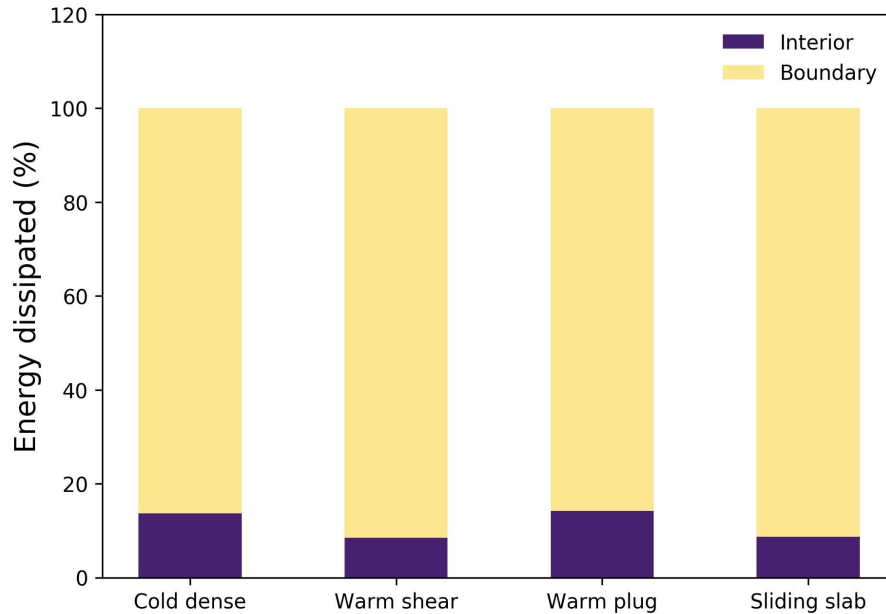

Figure 3. Energy dissipation inside the flow and through the boundary bed in the flows with the different flow regimes.

References:
- Gaume, J., Gast, T., Teran, J., van Herwijnen, A., and Jiang, C. (2018). Dynamic anticrack propagation in snow. *Nature Communications*, 9(1):1-10.
- Gracia, F., Villard, P., and Richefeu, V. (2019). Comparison of two numerical approaches (DEM and MPM) applied to unsteady flow. *Computational Particle Mechanics*, 6(4):591-609.

In section 4, the model strategy is applied to real cases with field measurements. It should be more clearly stated in each case what are the parameters that are set a priori and the one used for the calibration process. I suggest setting some stars in table 3 to distinguish calibrated parameters. The results are impressive with a very good agreement in general with field measures. The discrepancies are explained by the fact that MPM cannot entrain further material during the flow, that the turbulence dynamics in powder cloud is not modelled in MPM (some perspectives are set along this line although the frictional dissipation with air is not mentioned), that the measurement acquisition frequencies are not comparable between field and numerical data (in order to be more precise on this point, data could be presented with points instead of lines, for instance in Fig 14 where the velocity peak is much discussed.)

Reply: Following the reviewer's suggestion, it has been clarified in Lines 350-351 in the revised manuscript that the bed friction of the slope is the only calibrated parameter. In addition, a star has been used in Table 3 to notify the calibrated parameter. The adopted snow properties are fixed according to the description of the snow type in the literature, as detailed at Lines 345-350.

We thank the reviewer for pointing out the importance of frictional dissipation with air in the discussion of powder cloud. The corresponding sentence has been modified to reflect this aspect (Line 439).

Scattered points connected with a line have been used to plot the real measurement data in Figs 11-14 in the revised manuscript, which indeed offer more information on the measurement acquisition frequencies. Please note we still use lines for the MPM simulation data, since adding points does not differ much from the pure lines because the points overlap with one another as shown in Fig. 4 (Fig. 14 in the manuscript) below.
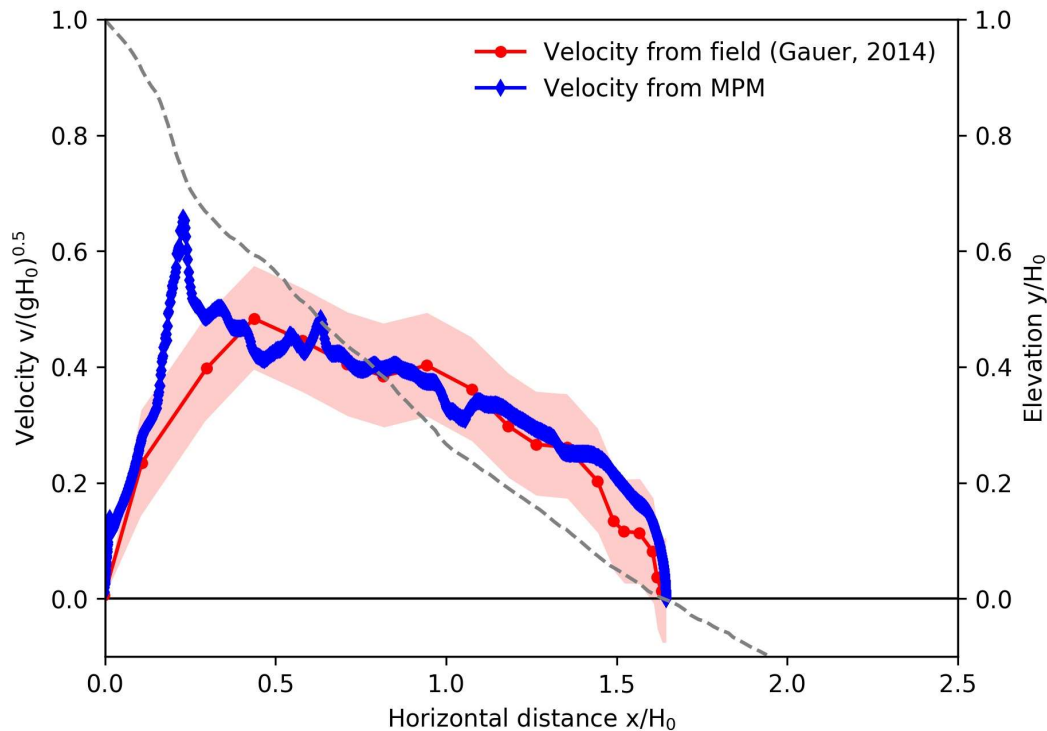

Figure 4. Front velocity distribution along the flow path for Case IV: Ryggfonn 2006-05-02 (Stryn, Norway). Drop height H_0 = 303 m.

The conclusion summarises the main qualitative results. A very interesting discussion is proposed at the end for the future work towards real geometry in 3D (MPM tools already exist in 3D, thus it is mainly a matter of computational time), to introduce in the MPM tool a constitutive law dedicated to powder cloud and its interaction with the dense part (the air friction is not mentioned here).

Reply: The air friction has been added (Line 439).

Overall the contribution is very well written, clear and well organised. The results and analysis are well documented, except the few points mentioned in bold in this review which need to be addressed for the final version. The work is original and provides an interesting step towards the prediction of snow avalanche propagation conditions.

Reply: We thank the reviewer for his constructive comments that helped us to improve the quality of our paper.

Response to Reviewer #2's comment

We thank Referee #2 for his or her insightful comments and helpful advice, which increase the quality of our paper. The following provides our point-to-point responses to the general comments, specific comments, and technical corrections from the reviewer.

General comments:

The paper presents a novel application of the authors recently developed approaches, successfully combining experimental findings on the flow regime evolution in snow avalanches and respective modelling approaches. The authors reach the goal of showing the models ability to replicate different flow regimes (and the associated flow characteristics, such as velocity, ...) by tuning the corresponding material parameters.

One point that could be enhanced in my eyes is the discussion of the role and connection between the numerical method/solver and the applied flow/material model. As the title states, the paper aims at the identification of the mechanical rather than the numerical origin of flow regimes in snow avalanches. However, the numerical method/solver (MPM) is often highlighted and associated with the success of the modeling results rather than the corresponding material model (see comments below).

Overall the paper is very well written and includes helpful figures with corresponding supplementary material (with some small exceptions mentioned below). This valuable contribution is of high quality, enjoyable to read and fits to the scope of TC.

Reply: We thank this reviewer for the encouraging comments. Regarding the numerical framework and the material model, this study indeed focuses on the material model, as we mainly investigate the effect of material property in addition to slope geometry. The relation between the numerical framework and the material model has been clarified in the revised manuscript as detailed in the reply of specific comment 2 below.

Specific comments:

1. p2 l 41-51 and section 2.1: could you include a comment what the main differences (e.g. 2d/3d, depth resolved/averaged, ...) are to the classical, numerical approaches that are used in common simulation software that you also cite throughout your paper (such

as Christen et al. (2010)). In particular the similarities and/or differences are to other particle based methods such as SPH (which are also used for classical shallow water 2d avalanche modelling Sampl and Zwinger (2004)) would probably be interesting for the reader to also interpret the future potential of the MPM methods (see conclusions).

References:
Christen, M., Kowalski, J., and Bartelt, P. (2010). RAMMS: Numerical simulation of dense snow avalanches in three-dimensional terrain. Cold Regions Science and Technology, 63:1–14.
Sampl, P. and Zwinger, T. (2004). Avalanche simulation with SAMOS. Annals of Glaciology, 38(1):393–398.

Reply: We have provided further introduction of existing numerical approaches for snow avalanche modelling in the revised manuscript (Lines 43-59), including 2D, 3D, and particle-based continuum methods, as follows.

Popular classical numerical tools for modelling snow avalanches primarily apply two-dimensional (2D) depth-averaged methods based on shallow water theory (Naaim et al., 2013; Rauter et al., 2018), which fail to capture important flow characteristics along the surface-normal direction such as velocity distribution (Eglit et al., 2020). Nevertheless, 2D models are computationally efficient and provide acceptable accuracy, which serve as a powerful tool in many applications like hazard mapping. In comparison, three-dimensional (3D) simulations can fully resolve flow variations in all dimensions, which consequently require longer computation time. In recent years, particle-based continuum methods, including Smooth Particle Hydrodynamics (SPH), Particle Finite Element Method (PFEM), and Material Point Method (MPM), have gained increasingly popularity in avalanche modelling, as they are able to easily handle large deformations and discontinuities (Abdelrazek et al., 2014; Salazar et al., 2016; Gaume et al., 2018). In particular, MPM has proven to be an effective and efficient tool in investigating snow (Stomakhin et al., 2013; Gaume et al., 2018). Compared with SPH where boundary conditions are challenging to generalize, MPM can readily address complex boundaries (Raymond et al., 2018). Moreover, MPM does not suffer from the time consuming neighbor searching that is inevitable in many mesh-free approaches like SPH (Abdelrazek et al., 2014). Both PFEM and MPM use a set of Lagrangian particles and a background mesh to solve mass and momentum conservation of a system. In contrast to PFEM, each particle in MPM has fixed mass, as it allows to naturally guarantee mass conservation. However, the fixed mass meanwhile leads to difficulty in adding or removing particles from the system (Larsson et al., 2020). The computational cost of MPM is lower than that of PFEM according to simulations with same formulation (Papakrivopoulos 2018).

References:
- Abdelrazek, A. M., Kimura, I., and Shimizu, Y. (2014). Numerical simulation of a small-scale snow avalanche tests using non-Newtonian SPH model. *Journal of Japan Society of Civil Engineers*, 70(2):I_681-I_690.
- Eglit, M., Yakubenko, A., and Zayko, J. (2020). A review of Russian snow avalanche models-From analytical solutions to novel 3D models. *Geosciences*, 10(2):77.

- Gaume, J., Gast, T., Teran, J., van Herwijnen, A., and Jiang, C. (2018). Dynamic anticrack propagation in snow. *Nature Communications*, 9(1):1-10.
- Larsson, S., Prieto, J. M. R., Gustafsson, G., Häggblad, H. Å., and Jonsén, P. (2020). The particle finite element method for transient granular material flow: modelling and validation. *Computational Particle Mechanics*, 1-21.
- Mast, C. M., Arduino, P., Miller, G. R., and Mackenzie-Helnwein, P. (2014). Avalanche and landslide simulation using the material point method: flow dynamics and force interaction with structures. *Computational Geosciences*, 18(5):817-830.
- Naaim, M., Durand, Y., Eckert, N., and Chambon, G. (2013). Dense avalanche friction coefficients: influence of physical properties of snow. *Journal of Glaciology*, 59(216):771-782.
- Papakrivopoulos, V. (2018). *Development and Preliminary Evaluation of the Main Features of the Particle Finite Element Method (PFEM) for Solid Mechanics*. Master's thesis, Delft University of Technology.
- Rauter, M., Kofler, A., Huber, A., and Fellin, W. (2018). faSavageHutterFOAM 1.0: depth-integrated simulation of dense snow avalanches on natural terrain with OpenFOAM. *Geoscientific Model Development*, 11:2923-2939.
- Raymond, S. J., Jones, B., and Williams, J. R. (2018). A strategy to couple the material point method (MPM) and smoothed particle hydrodynamics (SPH) computational techniques. *Computational Particle Mechanics*, 5(1):49-58.
- Salazar, F., Irazábal, J., Larese, A., and Oñate, E. (2016). Numerical modelling of landslide-generated waves with the particle finite element method (PFEM) and a non-Newtonian flow model. *International Journal for Numerical and Analytical Methods in Geomechanics*, 40(6):809-826.
- Stomakhin, A., Schroeder, C., Chai, L., Teran, J., and Selle, A. (2013). A material point method for snow simulation. *ACM Transactions on Graphics (TOG)*, 32(4):1-10.

2. p5 line 106, Table 1: here you particularly highlight the parameters for the MPM modeling. To me it appears that this could be misleading. All parameters refer to the material model (section 2.2.). No numerical parameters are discussed therefore the it would be interesting to: 1) comment the role of the numerical parameters and how they were chosen and to 2) clarify the role/interplay of the numerical technique and the material model (see comment on paper title above).

Reply: Indeed, the parameters in Table 1 include snow parameters. In addition to that, the information of slope geometry is also listed. Numerical parameters (i.e. mesh size, time step, and frame rate) have been added to Table 1 in the revision (Page 6). To avoid the confusion of "MPM model" and "material model", "Model parameters" in the title of Table 1 has been revised to "Parameters".

1) Numerical parameters govern the accuracy and stability of the modelling. The determination of the adopted numerical parameters (i.e. background mesh size, time step, and frame rate) has been detailed in Lines 138-140. The size of the background Eulerian mesh in MPM is selected to be small enough to guarantee the simulation accuracy and resolution, and meanwhile be large enough to shorten the computation time. The time step is constrained by the CFL condition and the elastic wave speed to secure the simulation stability. The simulation data are exported every 1/24 s.

2) The relation between the numerical framework and the material model has been clarified at Lines 93-98. Different material models can be implemented to the MPM numerical framework to simulate different processes. For example, a non-associated Mohr-Coulomb model was applied to model landslide and dam failure (Zabala and Alonso, 2011; Soga et al., 2016), and a non-associated Drucker-Prager model was used to simulate sand (Klár et al., 2016). In this study, we specifically use the associated Modified Cam Clay model developed for snow, which reproduces mixed-mode snow fracture and compaction hardening (Gaume et al., 2018). The important role of the material/constitutive model has also been clarified in Lines 67-68, 71.

References:
- Klár, G., Gast, T., Pradhana, A., Fu, C., Schroeder, C., Jiang, C., and Teran, J. (2016). Drucker-prager elastoplasticity for sand animation. *ACM Transactions on Graphics (TOG)*, 35(4):1-12.
- Gaume, J., Gast, T., Teran, J., van Herwijnen, A., and Jiang, C. (2018). Dynamic anticrack propagation in snow. *Nature Communications*, 9(1):1-10.
- Soga, K., Alonso, E., Yerro, A., Kumar, K., and Bandara, S. (2016). Trends in large-deformation analysis of landslide mass movements with particular emphasis on the material point method. *Géotechnique*, 66(3):248-273.
- Zabala, F., and Alonso, E. E. (2011). Progressive failure of Aznalcóllar dam using the material point method. *Géotechnique*, 61(9):795-808.

3. p7 line 145: Could you briefly explain a bit more what this threshold means and if or if not this is connected to the (numerical?) fluctuations that appear e.g. in Figure 3 b) around 5s for the cold dense and 7.5-10s for the warm shear simulations?

Reply: 1% of the particles at the flow front is excluded in the determination of the front position, because scattered particles are observed at the flow front in some of the flows (i.e. the warm shear flow and sliding slab flow in supplementary video 2). These scattered particles separate from the main body of the flow and do not reflect the actual front of the flow. Further clarification has been provided in Lines 181-184 to address this comment.

The sharp drop appeared in the front evolution of the cold dense flow at around 5 s is chiefly due to the change of the slope geometry, since the flow front enters the connecting arc zone at around 5 s. The fluctuations observed in the warm shear case from 7.5 s are mainly because of the discrete nature of the granules at the front of the flow (see supplementary video 1). The above discussion has been added to Lines 205-208, 214-215 in the revision.

4. p15 line 276: Could you briefly comment on what the plateau stage means and if or if not any of the avalanches reach some kind of final velocity / steady state?

Reply: Indeed, the maximum velocity of a flow v_{max} at the plateau stage reaches the theoretical prediction v_{max}^{b} with consideration of a rigid block sliding on a frictional bed. This means the maximum velocity is controlled by the frictional behaviour between the flow and the bed, which has been clarified in Lines 336-339.

5. p16 l 291, ...To calibrate and benchmark our MPM modeling...: is this really a calibration or rather a parameter variation/test with respect to the material / flow model rather than the numerical MPM approach?

Reply: Calibration of numerical modelling covers different parameters, including those from physical models implemented in the numerical framework (e.g. friction in Blagovechshenskiy et al. (2002)). In this study, we calibrated the MPM modelling by changing the bed friction, according to the data reported in the literature. "MPM modelling" here denotes the entire MPM simulation framework composed of the MPM numerical scheme and the material model. To avoid the confusion, it has been further specified in Lines 350-351 that the bed friction is the calibrated parameter. Please note the adopted snow properties are based on the description of the snow type in the literature, as described in Lines 345-350.

Reference:
- Blagovechshenskiy, V., Eglit, M., and Naaim, M. (2002). The calibration of an avalanche mathematical model using field data. *Natural Hazards and Earth System Science, Copernicus Publications on Behalf of the European Geosciences Union,* 2(3/4):217-220.

6. p16 l 307-310: I think here you have to clarify in more detail: 1) how are the avalanche velocities measures (different measurement techniques will lead to different velocities (front / core), see e.g. Rammer et al. (2007); Gauer et al. (2007)) and 2) if the measurements are comparable are the simulated velocities transformed correspondingly such they can be directly compared to the measurements (see e.g. Fischer et al. (2014))?

References:
Fischer, J. T., Fromm, R., Gauer, P., and Sovilla, B. (2014). Evaluation of probabilistic snow avalanche simulation ensembles with Doppler radar observations. Cold Regions Science and Technology, 97(0):151–158.
Gauer, P., Kern, M., Kristensen, K., Lied, K., Rammer, L., and Schreiber, H. (2007). On pulsed Doppler radar measurements of avalanches and their implication to avalanche dynamics. Cold Regions Science and Technology, 50(1):55–71.
Rammer, L., Kern, M., Gruber, U., and Tiefenbacher, F. (2007). Comparison of avalanche velocity measurements by means of pulsed Doppler radar, continuous wave radar and optical methods. Cold Regions Science and Technology, 50(1-3):35–54.

Reply: It has been clarified in Line 353 that different measurement techniques were used to obtain the front velocity, including Doppler radar devices and photo analyses. Particularly, continuous wave Doppler-radar was employed for the avalanches in Case I and Case II (Line 365). Pulsed Doppler-radar was used for the avalanche in Case III (Line 375). Timed photographs were used for the avalanches in Case IV (Line 382) and Case V (Line 391).

It is noticed that different measurement approaches may give different velocities, which are generally consistent with one another (Rammer 2007). The comparison basis

between velocities from numerical modelling and real measurements is sometimes questionable (Fischer et al., 2014; Rauter and Köhler, 2020). For example, depth-averaged velocities from numerical modelling cannot be directly compared to peak intensity velocities from Doppler radar measurements (Rauter and Köhler, 2020). In this study, the front velocity from MPM is determined as the approach velocity (Rauter and Köhler, 2020), which is calculated from the front position evolution with time and is assumed to be comparable with the data from the different measurement techniques. The approach velocity has a different definition from the velocity at the flow front, although their values are almost the same in our simulations as shown in Figs 5-9 below. The above discussion has been added to Lines 353-361.

References:

- Fischer, J. T., Fromm, R., Gauer, P., and Sovilla, B. (2014). Evaluation of probabilistic snow avalanche simulation ensembles with Doppler radar observations. *Cold Regions Science and Technology*, 97:151-158.
- Rammer, L., Kern, M. A., Gruber, U., and Tiefenbacher, F. (2007). Comparison of avalanche-velocity measurements by means of pulsed Doppler radar, continuous wave radar and optical methods. *Cold Regions Science and Technology*, 50(1-3):35-54.
- Rauter, M., and Köhler, A. (2020). Constraints on Entrainment and Deposition Models in Avalanche Simulations from High-Resolution Radar Data. *Geosciences*, 10(1):9.
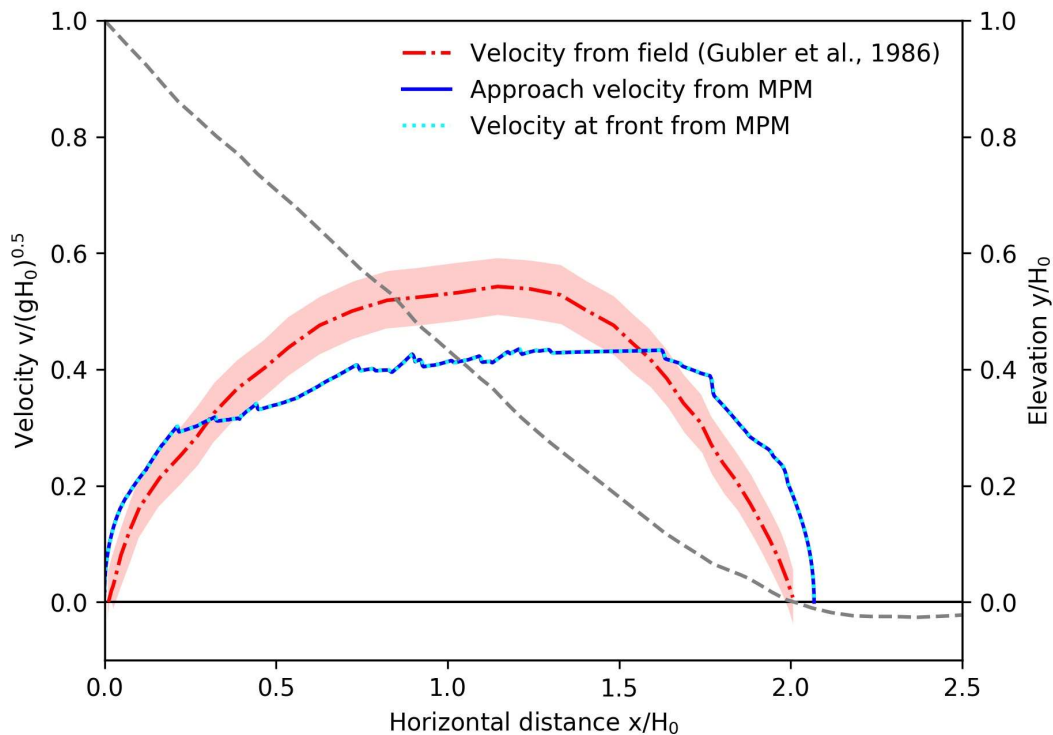
Figure 5. Front velocity distribution along the flow path for Case I: Weissfluh-Northridge 1982-03-12 a1 (Davos, Switzerland). Drop height H_0 = 236 m.
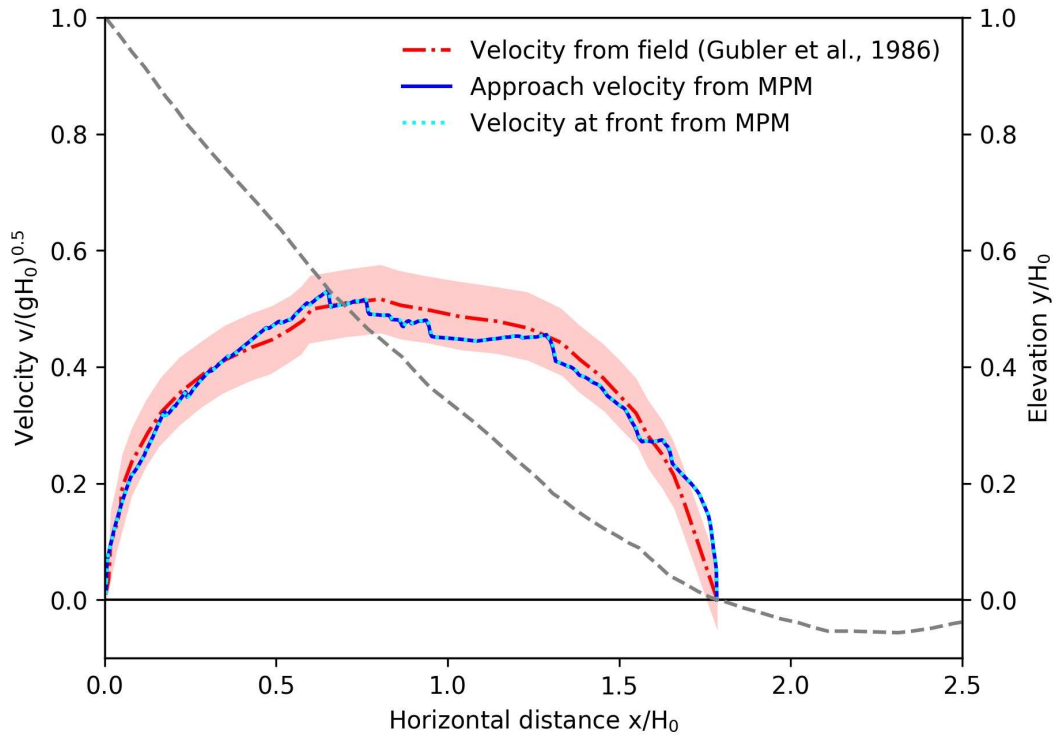
Figure 6. Front velocity distribution along the flow path for Case II: Weissfluh-Northridge 1982-03-12 a2 (Davos, Switzerland). Drop height H_0 = 177 m.
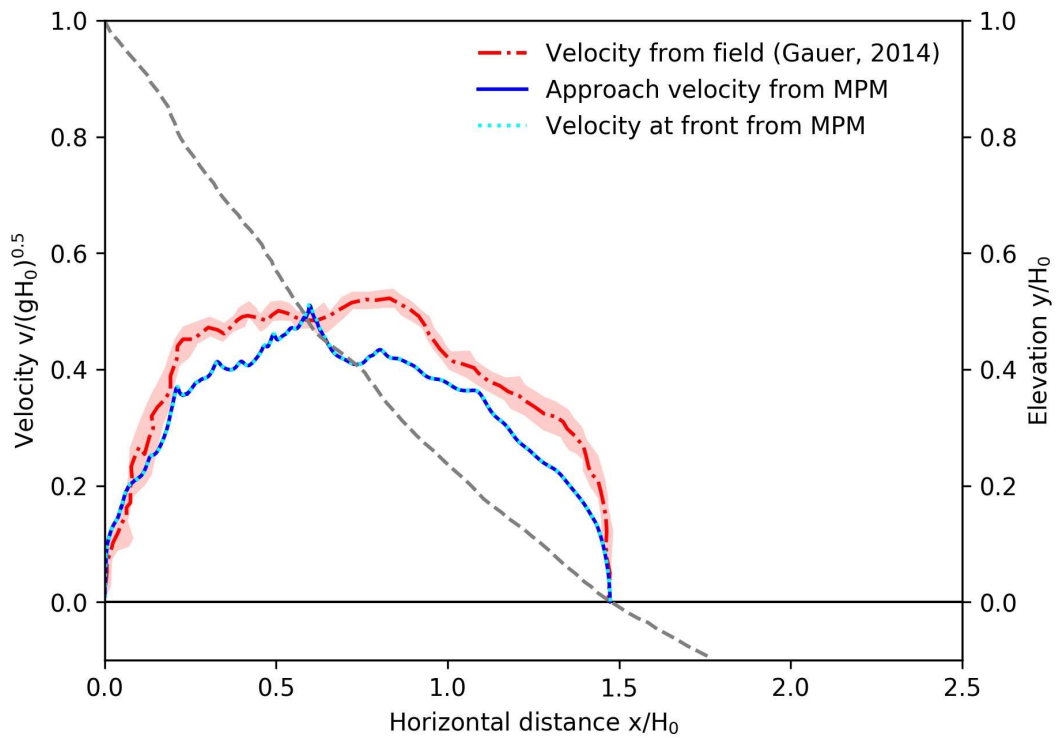

Figure 7. Front velocity distribution along the flow path for Case III: Himmelegg 1990-02-14 (Alberg, Austria). Drop height H_0 = 352 m.
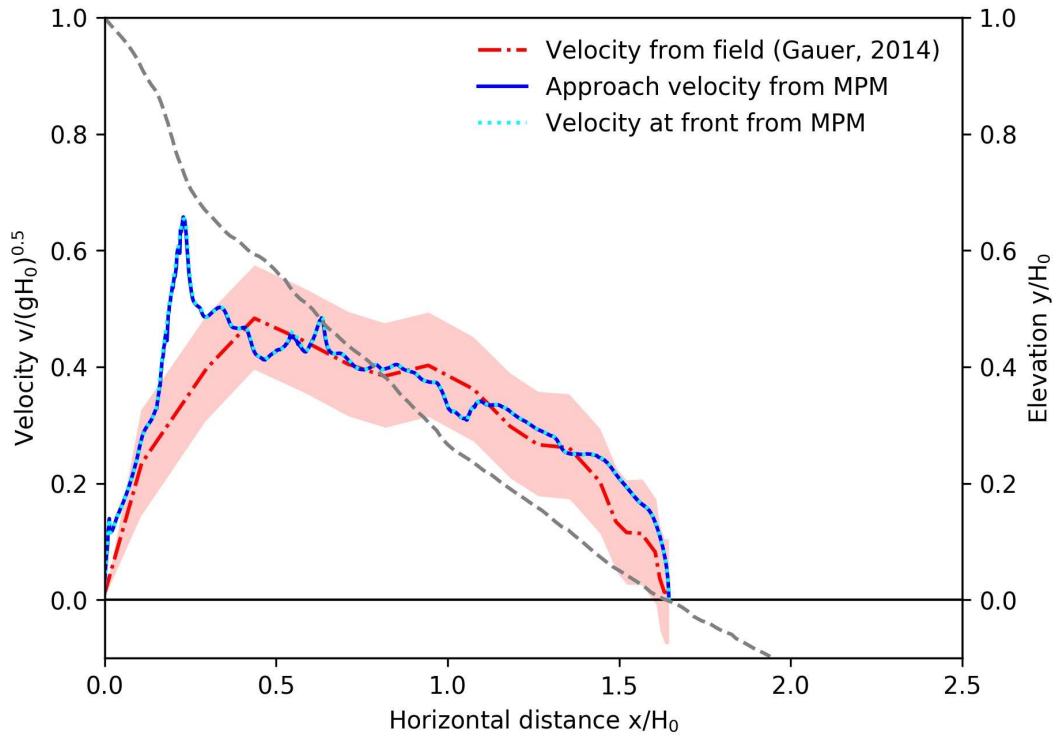
Figure 8. Front velocity distribution along the flow path for Case IV: Ryggfonn 2006-05-02 (Stryn, Norway). Drop height $H_0 = 303$ m.
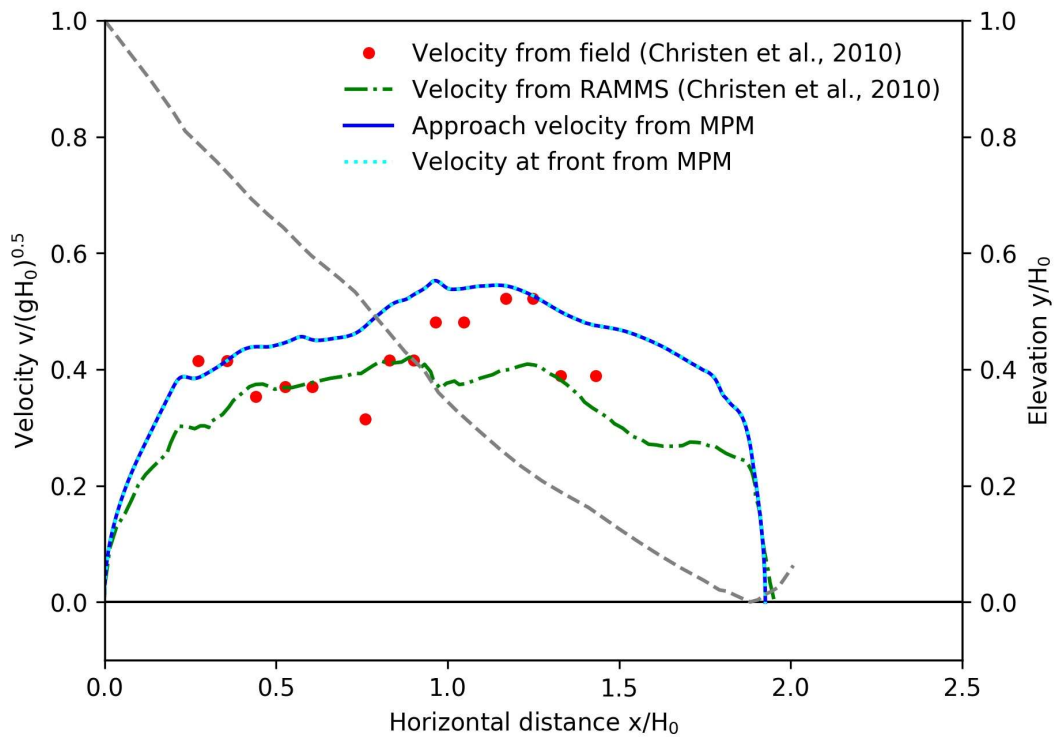

Figure 9. Front velocity distribution along the flow path for Case V: VdlS 2003-01-31 (Sion, Switzerland). Drop height $H_0 = 1246$ m.

Technical corrections:

Generally text and Figures are clear and the supplementary material is very helpful. Possible corrections include:

1. Figure2 and supplementary material: Fig2 is missing a spatial scale and the corresponding video is missing a legend (velocity/epsilon scale) as well as a spatial and temporal scale.

Reply: Spatial scale has been added to Fig. 2. The supplementary videos have been revised to include spatial and temporal scale as well as legend.

2. Figures 11-15 and supplementary material: absolute scales are missing and prohibit valuable data interpretation (at least total fall height should be stated in a Table or the caption).

Reply: Drop height has been clarified in the caption of Figs 11-15 and added to the supplementary data.

3. Wording: α should be referred to as runout angle.

Reply: "α angle" has been revised to "runout angle".

4. Wording: H/L and H0/L0 should be referred to the other way around (H/L=tan α is usually the convention why H/L refers to the topography inclination in this paper).

Reply: The definitions of H/L and H0/L0 have been exchanged.

5. Wording: what the authors refer to as "benchmark" appears more as a model "test" to me.

Reply: "MPM model is benchmarked" in the abstract has been revised to "MPM modeling is calibrated and tested" (Line 18). "To calibrate and benchmark our MPM modeling" in Line 342 has been modified to "To testify the capability of the MPM modeling in capturing key dynamic features (i.e. front velocity and position) of snow avalanches" (Lines 342-343).

6. Wording: please check by a native speaker if the choice of plural/singular is appropriate throughout the paper (e.g. behaviours, literatures, terrains, ...).

Reply: Thanks for the reminder. We have checked and revised the words with a native speaker.

Response to Reviewer #3's comment

We thank Referee #3 for his or her detailed comments and valuable suggestions, which helped us to improve the quality of the paper. Our point-to-point replies to the comments of the reviewer are summarized below.

The paper presents a systematic approach to evaluate the potential of the Material Point Method (MPM) for snow avalanches. The MPM method provides the possibility to account for different flow regimes of the avalanche flow in rather a novel approach.

In a first step the paper concerns avalanche on a selection of very simple geometries (At this point one could have considered a variety of parabolic track as this might be closer to Nature). The authors present a nice comparison of the influence of various parameters which would determine the flow regime.

Reply: We thank this reviewer for the suggestion on the parabolic track, which could be interesting and more realistic for future studies on snow avalanches with MPM modelling. This has been added to Lines 434-435 in the discussion.

I do have slight problems with section 3.3.2. First of all, the main idea behind so-called alpha-beta model (Lied and Bakkehoi, 1980) is that the runout angle alpha is proportional the beta angle, which is a measure of the mean slope angle. Hence there is no dependency on a length scale in the runout. Furthermore, solely considering the alpha angle involves little information without the corresponding beta angle. Having said that, Fig. 8 and Fig. 9 are not that easy to understand. For example, even though the velocities Fig. 9 seem to correspond somehow with the measurements, their origin (frictional behavior) might be rather different. E.g. the velocity of 70 m/s in the simulations correspond to nearly free fall velocity (2gH)ˆ.5 whereas as the measured one is close to (gH/2)ˆ.5. Hence there is a mix up in the comparison.

Reply: The following offers our point-to-point response to the comments on section 3.3.2.

1) Dependency of α on length scale: We agree that the runout angle α highly depends on the mean slope angle β. According to Lied and Bakkehøi (1980), the following correlation between α and β was obtained based on 111 avalanches

$$\alpha = 0.97\beta - 1.4°$$

with a standard deviation of 3.5° and R = 0.88. However, a more accurate prediction of α was reported as follows in Lied and Bakkehøi (1980)

$$\alpha = (6.2 \times 10^{-1} - 2.8 \times 10^{-1} Hy'')\beta + (1.9 \times 10^{1} Hy'' - 2.3)° + 1.2 \times 10^{-1}\theta$$

which has a standard deviation of 2.3° and R = 0.95. H is the total vertical displacement. y'' is the terrain profile of the avalanche path described by the second derivative. θ is the inclination of the starting zone (Note the θ in Lied and Bakkehøi (1980) has a different definition with the slope angle θ in our study). Thus, the runout angle also depends on the length scale of the avalanche path in addition to the

mean slope. As stated in Lied and Bakkehøi (1980), "*The most important parameter is the β. Hy'' is also an important parameter*".

2) Discussion of α without mentioning β: As reviewed above, the average slope angle β is a very important factor controlling the runout angle α. The origin/reason for proposing β is to describe the mean slope angle of a complicated and irregular flow path which is normally the case in reality. In our study, ideal slopes are used for the sensitivity study, whose mean slope angle β is very close to their actual slope angle (θ in our manuscript). We initially discussed the effect of θ without mentioning β to avoid the repetition. The relation between β and θ has been clarified in Lines 311-313 in the revised manuscript. In addition, it is found that the positive correlation between the maximum runout angle and the slope angle from MPM in Fig. 8 agrees with the α-β model, which has been mentioned in Lines 313-314.

3) Comparison of flow velocities from MPM and real measurements: As mentioned in Lines 316-317, the real avalanche with a velocity of 70 m/s was a powder snow avalanche, whose dense core can be captured by the current MPM model while the powder cloud is beyond the scope of this study. We agree that the high velocities (close to 70 m/s) from the real avalanche and the simulated avalanche come from different physical processes. The high velocity of the real avalanche is resulted from the large drop height (1940 m from McClung and Gauer (2018)). In contrast, the high velocity of the simulated avalanche is mainly controlled by the properties (low friction and low cohesion) of the flow. While we observe a generally fair agreement of the MPM and field data in Fig. 9, a quantitative comparison would require full consistency of the model setup (e.g. drop height, flow properties), as we did in Section 4 of the paper. Our main motivation here is to show the influence of mechanical (M and β) and geometrical (θ and L_0) properties on the v_{max}-α relationship and give a new insight to the negative correlation observed from the data in McClung and Gauer (2018) (Lines 320-324).

   According to the relation between the flow velocity and the drop height reported for real snow avalanches (Gauer, 2014), the high flow velocity close to 70 m/s obtained with a drop height of 211.2 m from the MPM simulation might not be realistic for snow avalanches. It has been clarified in Lines 424-426 that the adopted material parameters are designed to study a wide range of different material properties, while the cases with very low friction M and cohesion β leading to the very high velocity might not be realistic for snow avalanches. The material parameters need to be carefully calibrated for investigation of real snow avalanches.

References:
- Gauer, P. (2014). Comparison of avalanche front velocity measurements and implications for avalanche models. *Cold Regions Science and Technology*, 97:132-150.
- Lied, K., and Bakkehøi, K. (1980). Empirical calculations of snow–avalanche run–out distance based on topographic parameters. *Journal of Glaciology*, 26(94):165-177.

- McClung, D. M., and Gauer, P. (2018). Maximum frontal speeds, alpha angles and deposit volumes of flowing snow avalanches. *Cold Regions Science and Technology*, 153:78-85.

Finally, the authors present a promising comparison between simulations and real avalanche measurements.

It would be interesting to see how the model would behave when erosion and entertainment is also considered.

Some minor remarks can be found in the attachments.

Reply: We appreciate the reviewer's interest in the performance of the model with consideration of erosion and entrainment. We also consider entrainment as an interesting and very important process in snow avalanches, and will be the topic of our next study using MPM (Lines 439-444).

Specific comments:

1. Line 9: "Each of the flow regimes shows" should be "Each of the flow regimes show"?

Reply: Since "each" is our subject, "shows" is used.

2. Line 13: "scaled α angle", an angle can hardly be scaled.

Reply: The scaled α angle refers to the dimensionless α*. This notation has been clarified in Line 331.

3. Line 14: "It is found …" to "It is found that …".

Reply: Revised.

4. Line 29: "classified" to "considered".

Reply: Revised.

5. Line 30: Delete "including".

Reply: "including" has been replaced by "namely,".

6. Line 30: "Recent study" to "A recent study".

Reply: Revised.

7. Line 36: "tools", model (I think is the better word here).

Reply: Thanks for the rewording. Revised.

8. Fig. 2 caption: Add "(Tab. 1, Group II)".

Reply: Added.

9. Line 146: "front position" to "the front position".

Reply: Revised (Line 180).

10. Fig. 3 caption: Add "(Tab. 1, Group II)".

Reply: Added.

11. Fig. 3: Which mu value is used in the calculation of v_{max}^b?

Reply: Thanks for the question. The value of mu is 0.5, which has been added to Lines 191-192 and Table 1.

12. Fig. 4 caption: Add "(Tab. 1, Group II)".

Reply: Added.

13. Fig. 5 caption: Add "and lengths L".

Reply: The data with different lengths L (L_0 in the revised manuscript) are not included in Fig. 5. They are plotted in Fig. 6.

14. Fig. 6 caption: Add "slope angles".

Reply: The data with different slope angles are not included in Fig. 6. They are plotted in Fig. 5.

15. Line 226: "which hints an analogous physical rule behind the trend", what is the physical rule you are thinking of?

Reply: As described in Lines 267-288, the data from the different groups of simulations give a similar trend, which drives us to normalize the results and find the analogous physical rule behind the similarity. Based on the normalized results in Fig. 7, there are different physical processes governing the data in the different regions. The maximum velocity of the cases close to the zero line in Fig. 7 is controlled by the friction between the flow and the bed (Lines 280-282). On the other hand, the velocity of the cases with small M and β in Fig. 7 is governed by the snow properties (Lines 282-286). Furthermore, the velocity of the cases far below the zero line in Fig. 7 is due to an acceleration smaller than the theoretical one obtained from a block sliding over a frictional bed (Lines 286-288). All the cases from the different groups follow and share these three physical processes.

16. Figs 8&9: I'm wondering how the graphs would look like for H = L*tan(slope) combined.

Reply: We tried to plot all the data in one figure for the varying H (H_0 in the revised manuscript and hereafter) as shown in Fig. 10 below. The increase of drop height does not necessarily give an increasing maximum velocity if we compare the data with H_0 = 73.5 m and the data with H_0 = 132.0 m. This is because these two groups do not have the same slope angle in this study. Thus, it is necessary to separately discuss the groups with a fixed slope angle and the groups with a fixed horizontal length, as we did in Figs 8&9. It is mentioned in Lines 133-135 in the revised manuscript that, instead of fixing the horizontal length L (L_0 in the revised manuscript) when the slope angle is changed (Groups I, II, III in Table I), one could fix the vertical drop height H_0 and change the horizontal length.
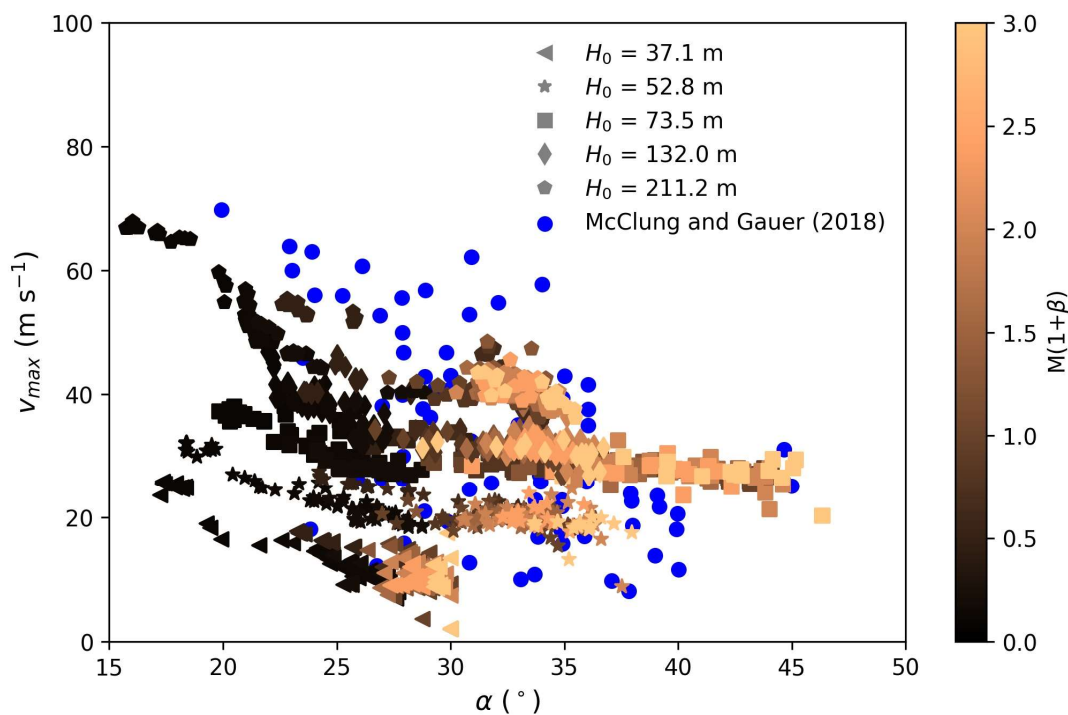

Figure 10. Evolution of the maximum velocity with α for varying drop height H_0.

17. Line 355: "Both slope angle and path length have a positive correlation with the maximum front velocity on the slope", this is not that surprise as total Drop height H = L*tan(slope). and Umax \prop f(H).

Reply: We agree that the total drop height should have a similar effect as the horizontal length L and the slope angle θ. The reason that we separately discuss the slope angle and the path length is that we have both the slope angle and the path length in the calculation of the theoretical maximum velocities v_{max}^b and v_{max}^f (Lines 190-193).

The mechanical origin of snow avalanche dynamics and flow regime transitions

Xingyue Li[1], Betty Sovilla[2], Chenfanfu Jiang[3], and Johan Gaume[1,2]

[1]School of Architecture, Civil and Environmental Engineering, Swiss Federal Institute of Technology, Lausanne, Switzerland
[2]WSL Institute for Snow and Avalanche Research, SLF, Davos, Switzerland
[3]Computer and Information Science Department, University of Pennsylvania, Philadelphia, USA

Correspondence: Johan Gaume (johan.gaume@epfl.ch)

Abstract. Snow avalanches cause fatalities and economic damages. Key to their mitigation entails the understanding of snow avalanche dynamics. This study investigates the dynamic ~~behaviors~~ behavior of snow avalanches, using the Material Point Method (MPM) and an elastoplastic constitutive law for porous cohesive materials. By virtue of the hybrid Eulerian-Lagrangian nature of MPM, we can handle processes involving large deformations, collisions and fractures. Meanwhile, the elastoplastic model enables us to capture the mixed-mode failure of snow, including tensile, shear and compressive failure. Using the proposed numerical approach, distinct behaviors of snow avalanches, from fluid-like to solid-like, are examined with varied snow mechanical properties. In particular, four flow regimes reported from real observations are identified, namely, cold dense, warm shear, warm plug and sliding slab regimes. Moreover, notable surges and roll-waves are observed peculiarly for flows in transition from cold dense to warm shear regimes. Each of the flow regimes shows unique flow characteristics in terms of the evolution of the avalanche front, the free surface shape, and the vertical velocity profile. We further explore the influence of slope geometry on the ~~behaviors~~ behavior of snow avalanches, including the effect of slope angle and path length on the maximum flow velocity, the ~~α~~ runout angle and the deposit height. Unified trends are obtained between the normalized maximum flow velocity and the scaled ~~α~~ runout angle as well as the scaled deposit height, reflecting analogous rules with different geometry conditions of the slope. It is found that the maximum flow velocity is mainly controlled by the friction between the bed and the flow, the geometry of the slope, and the snow properties. ~~In addition to the flow behavior before reaching the deposition zone, which has long been regarded as the key factor governing the α angle, we~~ We reveal the crucial effect of ~~the stopping behavior in the deposition zone~~ both flow and deposition behaviors on the runout angle. Furthermore, our MPM ~~model is benchmarked~~ modeling is calibrated and tested with simulations of real snow avalanches. The evolution of the avalanche front position and velocity from the MPM modeling shows reasonable agreement with the measurement data from literature. The MPM approach serves as a novel and promising tool to offer systematic and quantitative analysis for mitigation of gravitational hazards like snow avalanches.

1   Introduction

Snow avalanches have long been threatening infrastructures and human lives. Buildings, roads and railways can be severely damaged, causing ~~serious~~ profound economic losses. Moreover, the fatalities induced by snow avalanches are significant,

which are about 100 annually in the European Alps during the last four decades (Techel et al., 2016). Due to climate change, the frequency and risk of snow avalanches are still increasing (Choubin et al., 2019). It is thus of great importance to mitigate snow avalanche hazards, which highly relies on the understanding of their complex dynamic ~~behaviors~~behavior.

Snow can behave as a fluid or as a solid under different conditions, leading to distinct behaviors of snow avalanches in reality (Gaume et al., 2011; Ancey, 2016). Characterizing different flow regimes of snow avalanches ~~have~~has played a significant role in hazard mapping and design of mitigation measures (Gauer et al., 2008). Traditionally, two flow regimes were ~~classified~~ considered for snow avalanches, ~~including~~ namely, dense snow avalanches and powder snow avalanches. ~~Recent~~ A recent study by Köhler et al. (2018) highlighted the role of ~~the~~ snow temperature in classifying the flow regimes and extended the traditional classification. The starting, flowing and stopping signatures of snow avalanches were used to distinguish seven flow regimes, including four dense flow regimes, two powder flow regimes, and a snowball flow regime. Although the flow regimes have been identified based on macro flow ~~behaviors~~ behavior from the real measurements, their underlying physics remains unclear. Numerical and theoretical models can provide efficient and comprehensive analysis to shed light on the internal flow characteristics underpinning the macro flow ~~behaviors~~behavior, but are extremely challenging (Faug et al., 2018). To date, there has been no recognized ~~tools~~ model capable of capturing and analyzing the diverse behaviors of snow avalanches in a systematic and well-controlled way. Furthermore, the crucial effects of snow mechanical property and terrain geometry on snow avalanche dynamics have been widely recognized, but are sparsely investigated due to practical challenges. Only limited numerical and real-measurement studies were reported (Keshari et al., 2010; Fischer et al., 2012, 2015; Steinkogler et al., 2014).

Popular classical numerical tools for modeling snow avalanches primarily apply two-dimensional (2D) depth-averaged methods based on shallow water theory (Naaim et al., 2013; Rauter et al., 2018), which fail to capture important flow characteristics along the surface-normal direction such as velocity distribution (Eglit et al., 2020). Nevertheless, 2D models are computationally efficient and provide acceptable accuracy, which serve as a powerful tool in many applications like hazard mapping. In comparison, three-dimensional (3D) simulations can fully resolve flow variations in all dimensions, which consequently require longer computation time. In recent years, particle-based continuum methods, including Smooth Particle Hydrodynamics (SPH), Particle Finite Element Method (PFEM), and Material Point Method (MPM), have gained increasing popularity in avalanche modeling, as they are able to easily handle large deformations and discontinuities (Abdelrazek et al., 2014; Salazar et al., 2016; Gaume et al., 2018a). In particular, MPM has proven to be an effective and efficient tool in investigating snow (Stomakhin et al., 2013; Gaume et al., 2018a, b, 2019). Compared with SPH where boundary conditions are challenging to generalize, MPM can readily address complex boundaries (Raymond et al., 2018). Moreover, MPM does not suffer from the time consuming neighbor searching that is inevitable in many mesh-free approaches like SPH (Mast et al., 2014). Both PFEM and MPM use a set of Lagrangian particles and a background mesh to solve mass and momentum conservation of a system. In contrast to PFEM, each particle in MPM has fixed mass, as it allows to naturally guarantee mass conservation. However, the fixed mass meanwhile leads to difficulty in adding or removing particles from the system (Larsson et al., 2020). The computational cost of MPM is lower than that of PFEM according to simulations with same formulation (Papakrivopoulos, 2018).

60   This study applies ~~the Material Point Method (MPM)~~MPM in 2D (slope-parallel and slope-normal) to explore the distinct behaviors of snow avalanches and the key controlling factors of snow avalanche dynamics. To facilitate efficient computation and capture important flow features along the surface-normal direction, our 2D MPM modeling neglects variations along the flow width. MPM is a hybrid Eulerian-Lagrangian approach, which uses Lagrangian particles to track mass, momentum and deformation gradient, and adopts Eulerian background mesh to solve and update the motion of the particles. By virtue

65 of the hybrid Eulerian-Lagrangian nature of MPM, processes with large ~~deformation~~deformations, fractures, collisions and impacts can be well simulated (Mast et al., 2014; Gaume et al., 2018a, b, 2019). In addition, continuous solid-fluid phase transition and coexistence of solid-like and fluid-like behaviors can be captured with implementation of proper constitutive models (Stomakhin et al., 2013; Gaume et al., 2018a). MPM has been increasingly adopted to investigate gravity-driven flows like landslides, debris flows and avalanches (Soga et al., 2016; Abe and Konagai, 2016; Gaume et al., 2018a). This study will

70 highlight the capability of MPM in capturing different flow regimes of snow avalanches from fluid-like shear flow to solid-like sliding slab, by adopting a finite strain elastoplastic constitutive model. Furthermore, it will be demonstrated that the proposed numerical approach serves as a promising tool to systematically study the key influencing factors of snow avalanche dynamics, including snow mechanical property and slope geometry.

2   Methodology

75 ### 2.1   The Material Point Method (MPM)

Assuming a continuous material, MPM discretizes it into Lagrangian particles (material points) to trace mass, momentum and deformation gradient, and adopts Eulerian grids to solve the motion of the particles and update their states. In particular, the particle motion is governed by mass and momentum conservation as follows

$$\frac{D\rho}{Dt} + \rho\nabla\cdot\boldsymbol{v} = 0 \tag{1}$$

80

$$\rho\frac{D\boldsymbol{v}}{Dt} = \nabla\cdot\boldsymbol{\sigma} + \rho\mathbf{g} \tag{2}$$

where ρ is density, t is time, $\boldsymbol{v}$ is velocity, $\boldsymbol{\sigma}$ is the Cauchy stress, $\boldsymbol{g}$ is the gravitational acceleration. As the mass carried by each particle does not vary, the balance of mass is satisfied naturally. The momentum balance is solved with a regular background Eulerian grid mesh and the discretization of the weak form of Eq. (2). The explicit MPM algorithm by Stomakhin

85 et al. (2013) is applied with a symplectic Euler time integrator. Details of the adopted MPM time stepping algorithm can be found in Stomakhin et al. (2013); Jiang et al. (2016); Gaume et al. (2018a). Note compared to Gaume et al. (2018a), this study uses Affine Particle-In-Cell (APIC) method (Jiang et al., 2015), by which angular momentum is preserved in addition to linear momentum.

MPM relies on a continuum description and requires a constitutive model for the considered material. The Cauchy stress $\boldsymbol{\sigma}$ in Eq. (2) is related to the strain thorough an elastoplastic constitutive law as follows

$$\boldsymbol{\sigma} = \frac{1}{J}\frac{\partial \Psi}{\partial \boldsymbol{F}_E}\boldsymbol{F}_E^T \tag{3}$$

where Ψ is the elastoplastic potential energy density, $\boldsymbol{F}_E$ is the elastic part of the deformation gradient $\boldsymbol{F}$, and $J = \det(\boldsymbol{F})$. ~~The adopted elastoplastic constitutive law facilities the~~ Note that various constitutive models can be implemented into the framework of MPM to capture different materials and their distinct behaviors. For example, a non-associated Mohr-Coulomb model was applied to model landslide and dam failure (Zabala and Alonso, 2011; Soga et al., 2016), and a non-associated Drucker-Prager model was used to simulate sand (Klár et al., 2016). In this study, we use the associated Modified Cam Clay model developed for snow (Gaume et al., 2018a), which reproduces mixed-mode ~~failure of snow and is detailed in the following~~ snow fracture and compaction hardening.

2.2 Finite strain elastoplastic model

The elastoplastic model in this study is borrowed from Gaume et al. (2018a), which consists of a mixed-mode shear-compression yield surface, a hardening law, and an associative flow rule. We recall the main characteristics of the three key components. On the basis of laboratory experiments (Reiweger et al., 2015) and simulations based on X-ray computed tomography (Hagenmuller et al., 2015; Chandel et al., 2015; Srivastava et al., 2017), the yield surface is defined in the space of the $p - q$ invariants of the stress tensor as follows

$$y(p,q) = (1+2\beta)q^2 + M^2(p+\beta p_0)(p-p_0) \tag{4}$$

p is the pressure calculated as $p = -\text{tr}(\boldsymbol{\tau})/d$, where $\boldsymbol{\tau}$ is the Kirchhoff stress tensor and d is the dimension. q is the Mises stress defined as $q = (3/2\,\mathbf{s}:\mathbf{s})^{1/2}$, where ~~s~~ $\mathbf{s} = \boldsymbol{\tau} + p\mathbf{I}$ is the deviatoric stress tensor ~~equaling to $\boldsymbol{\tau} + p\mathbf{I}$~~ and $\mathbf{I}$ is the identity matrix. p_0 is the consolidation pressure and denotes the isotropic compressive strength. βp_0 is the isotropic tensile strength, where β reflects the cohesion. M is the slope of the critical state line, which characterizes the internal friction.

When the $p - q$ state of the material is inside ~~or on~~ the yield surface (i.e. ~~$y(p,q) \leq 0$~~ $y(p,q) < 0$), the material behaves elastically and follows Hooke's law (St Venant-Kirchhoff Hencky strain). Plastic behavior happens if ~~$y(p,q) > 0$~~ $y(p,q) = 0$. Depending on the volumetric plastic strain ϵ_v^p, hardening or softening is implemented by expanding or shrinking the yield surface according to the following hardening law

$$p_0 = K\sinh(\xi\max(-\epsilon_v^p, 0)) \tag{5}$$

where K is the bulk modulus and ξ is the hardening factor. Under compression ($\dot{\epsilon}_v^p < 0$), p_0 increases, leading to hardening and promoting compaction. Under tension ($\dot{\epsilon}_v^p > 0$), p_0 decreases, resulting in softening and allowing fracture.

A flow rule needs to be adopted when ~~the~~ plastic behavior occurs. Referring to Gaume et al. (2018a), this study uses ~~the~~ an associative plastic flow rule reported by Simo (1992) and Simo and Meschke (1993). The applied flow rule follows the principle of maximum plastic dissipation, which maximizes the rate of plastic dissipation. It is worth noting that the second

120   law of thermodynamics is fully satisfied by using the plastic model with the flow rule. More details can be found in Gaume et al. (2018a).

3   Snow avalanches on ideal slopes
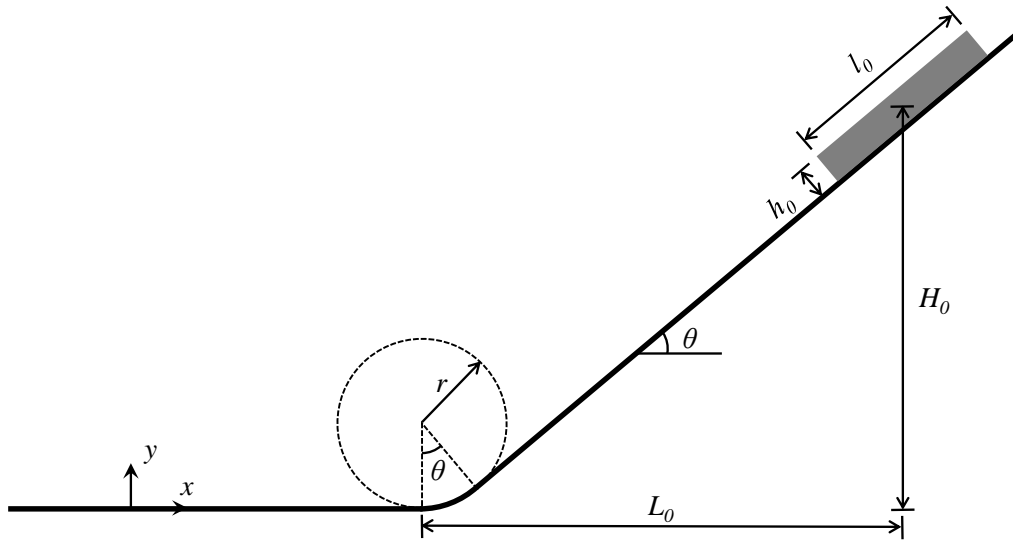
3.1   Model setup

Figure 1. Model setup for MPM modeling of snow avalanches on an ideal slope.

To examine the ~~behaviors~~ behavior of snow avalanches under a well-controlled condition, the setup with a rectangular snow
125   sample and an ideal slope is adopted as illustrated in Fig. 1. The snow sample is initially placed at the top of the slope, ~~which~~ and will flow down under gravity. The inclined slope is connected to the horizontal ground using a circular arc with a central angle equaling to the slope angle θ. The arc and the horizontal ground are named connecting arc zone and deposition zone in the following discussion, respectively. To investigate different flow regimes of snow avalanches, the properties of snow are systematically varied, including the friction coefficient M, the tension/compression ratio β, the hardening factor ξ, and the
130   initial consolidation pressure p_0^{ini}. In addition, the ~~effects of the~~ effect of slope angle θ and ~~the horizontal length L~~ horizontal length L_0 in Fig. 1 ~~are~~ is studied with five groups of simulations as summarized in Table 1. For each group, the snow properties are changed within the prescribed ranges. Groups I, II, III are conducted to study the influence of slope angle θ, whilst Groups II, IV, V are designed to examine the effect of the horizontal length ~~L. Note L/h_0, L/l_0, and L/r~~ L_0. When θ is varied in Groups I, II, III, the horizontal length L_0 is fixed and the drop height H_0 is adjusted as listed in Table 1. Alternatively, one
135   could fix the drop height H_0 and change the horizontal length L_0. Note L_0/h_0, L_0/l_0, and L_0/r are kept constant when ~~L~~

L_0 is varied in Groups II, IV, V, by changing h_0, l_0 and r accordingly. An increased ~~L~~ L_0 leads to the scale-up of the setup, resulting in the rise of the drop height ~~H~~ H_0. Detailed parameters adopted in the MPM simulations are summarized in Table 1. The size of the background Eulerian mesh in MPM is selected to be small enough to guarantee the simulation accuracy and resolution, and meanwhile be large enough to shorten the computation time. The time step is constrained by the CFL condition and the elastic wave speed to secure the simulation stability. The simulation data are exported every 1/24 s.

Table 1. ~~Model parameters~~ Parameters adopted ~~for~~ in the MPM simulations of snow avalanches on ideal slopes.

		Group I	Group II	Group III	Group IV	Group V
Snow	Density ρ (kg/m^{-3})	250	250	250	250	250
	Young's modulus E (MPa)	3	3	3	3	3
	Poisson's ratio ν	0.3	0.3	0.3	0.3	0.3
	Friction coefficient M [*]	0.1~1.5	0.1~1.5	0.1~1.5	0.1~1.5	0.1~1.5
	Tension/compression ratio β [*]	0.0~1	0.0~1	0.0~1	0.0~1	0.0~1
	Hardening factor ξ [*]	0.1~10	0.1~10	0.1~10	0.1~10	0.1~10
	Initial consolidation pressure p_0^{ini} (kPa) [*]	3~30	3~30	3~30	3~30	3~30
	Initial height h_0 (m)	2	2	2	5	8
	Initial length l_0 (m)	12	12	12	30	48
Slope	Bed friction coefficient μ	0.5	0.5	0.5	0.5	0.5
	Slope angle θ ($°$)	30	40	50	40	40
	Radius r (m)	10	10	10	25	40
	Drop height ~~H~~ H_0 (m)	37.1	52.8	73.5	132.0	211.2
	Horizontal length ~~L~~ L_0 (m)	65	65	65	162.5	260
Simulation control	Mesh size (m)	0.05	0.05	0.05	0.05	0.05
	Time step (s)	2.3×10^{-4}	2.3×10^{-4}	2.3×10^{-4}	2.3×10^{-4}	2.3×10^{-4}
	Frame rate (FPS)	24	24	24	24	24

[*] M values include 0.1, 0.5, 1.0, 1.5. β values include 0.0, 0.3, 0.6, 1.0. ξ values include 0.1, 0.5, 1.0, 10.0. p_0^{ini} values include 3 kPa, 12 kPa, 21 kPa, 30 kPa.

3.2 Typical flow regimes

In each group of our MPM simulations, four typical flow regimes are captured with the changing mechanical properties of snow. Fig. 2(a) shows four representative cases in Group II, where distinct flow regimes are observed with the different snow properties summarized in Table 2. From top to bottom, we observe Regime 1 to Regime 4. The flow in Regime 1 behaves as a fluid or a dry cohesionless granular flow, whose free surface is continuous. Since the height of the flow in Regime 1 is excessively small compared with the others, it is scaled up to be three times higher along the bed normal direction for better visualization in Fig. 2(a). Small surges are observed especially at the front of the flow in Regime 1. The flow in Regime 2 demonstrates a more fluctuated free surface and a discontinuous tail, due to the occurrence of a granulation process. The flow
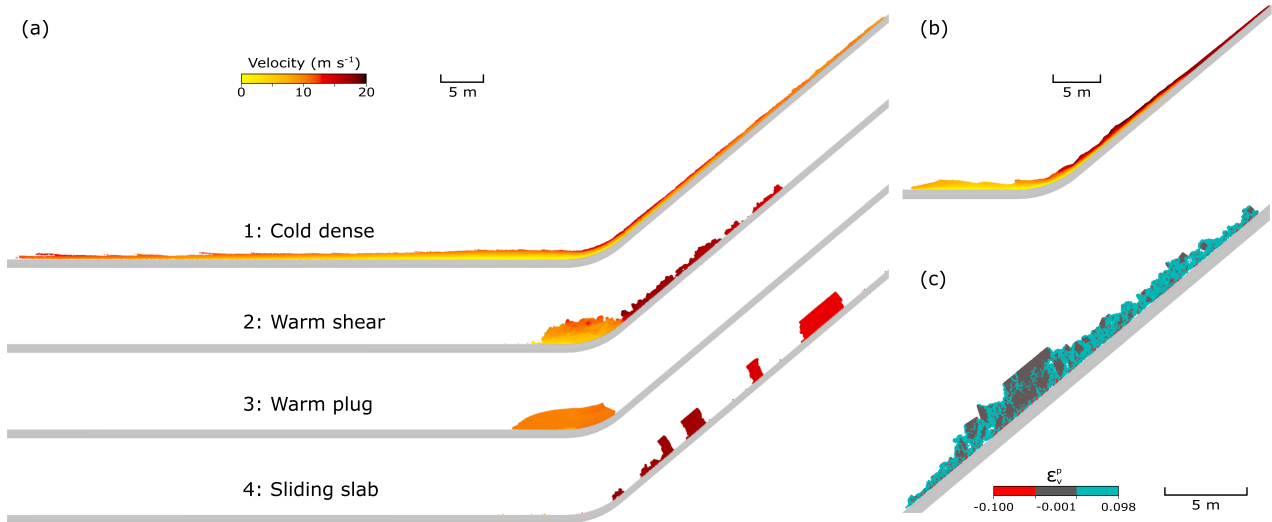
6

Figure 2. (a) Flows in four typical flow regimes captured at t = 8.3 s in the MPM simulations (Table 1, Group II). From top to bottom: cold dense, warm shear, warm plug and sliding slab. The cold dense flow is scaled up to be three times higher along the bed normal direction for better visualization. (b) A flow with surges and small granules in transition from cold dense regime to warm shear regime at t = 8.3 s. The color denotes velocity as in (a). (c) The early stage (t = 5.5 s) of the warm shear flow in (a). Videos of the simulations are provided as supplements.

height of the granular flow is higher compared with that of the flow in Regime 1, since the granules can be notably accumulated

150   in the connecting arc and deposition zones. The flow in Regime 3 demonstrates ductile ~~behaviors~~behavior, and slides down the slope and reaches the horizontal deposition zone with no significant deformation and no cracks. In contrast, clear cracks and broken pieces are noticed in the flow in Regime 4. The initial snow sample in Regime 4 breaks into multiple blocks shortly after its release from the slope.

      The four flow regimes in Fig. 2(a) show similar features with the identified flow regimes by Köhler et al. (2018) based on

155   the real measurements and observations, namely, cold dense, warm shear, warm plug, and sliding slab regimes. The detailed macro flow characteristics and internal shearing ~~behaviors~~ behavior of the flows will be discussed in the following section. The information of the energy of the flows is provided in Appendix A. In addition, flows in transition between the flow regimes can be captured as well. For example, Fig. 2(b) shows a flow in transition from cold dense to warm shear flow regimes, as it demonstrates the characteristics of both regimes. Significant surges and roll-waves occur in Fig. 2(b), showing similarity

160   with the cold dense flow. On the other hand, small granules are observed at the early stage of the flow (see ~~supplement~~ supplementary video 4), presenting characteristics of the warm shear flow. This transitional flow is modeled with $M\beta = 0.15$ ($M = 0.5$; $\beta = 0.3$), whose properties are in between of the cold dense and warm shear flows listed in Table 2. Although only one flow regime is characterized for each of the flows in Fig. 2(a), it is worth noting that a single snow avalanche may ~~have different flow behaviors and~~ display different flow regimes at its different ~~parts~~ locations and at different instants (Kern et al.,

165 2009). Fig. 2(c) shows the warm shear flow in Fig. 2(a) at its early stage (t = 5.5 s), where the red and blue materials are respectively in compression and tension and the dark gray denotes the initial state of the material. The red particles are hardly visible as they are located at the bottom layer of the flow, which indicates that the snow inside the core of the avalanche is mainly under tension or at the initial state. At t = 5.5 s, the flow demonstrates the characteristics of sliding slab, as the dark gray part slides along the slope and is seldom sheared. The initial sliding slab in Fig. 2(c) can indeed transform into the warm

170 shear flow in Fig. 2(a) after it reaches the deposition zone.

Table 2. Snow properties adopted in the MPM modeling of the flows in the four typical flow regimes.

Flow regime	M	β	ξ	p_0^{ini} (kPa)	βp_0^{ini} (kPa)	$M\beta$
Cold dense	0.1	0	1	3	0	0
Warm shear	1.5	0.3	10	30	9	0.45
Warm plug	0.5	1	0.1	12	12	0.5
Sliding slab	1.5	1	1	21	21	1.5

All the demonstrated flows in the four typical regimes share identical initial and boundary conditions except for the snow properties. From the simulations, it is clear that higher M and β gives a more frictional and cohesive flow, since they reflect the internal friction and cohesion, respectively. For instance, the M and β of the flow in the warm shear regime are higher than that of the cold dense regime, which facilitate the formation of the granules and the higher flow height. The hardening coefficient

175 ξ and the initial consolidation pressure p_0^{ini} also affect the flow ~~behaviors~~behavior, whose influence depends on the M and β according to our sensitivity study. As listed in Table 2, the tensile strength βp_0^{ini} and $M\beta$ consistently increase from the cold dense to the sliding slab flow regimes, which give indications on the possible underpinning factors controlling the transition of the flow regimes.

3.2.1 Front evolution

180 Fig. 3 illustrates the evolution of the front position and velocity for the flows in the four typical flow regimes in Fig. 2(a). ~~The front position~~ In some of the simulated flows, scattered particles are observed at the flow front (i.e. the warm shear flow and sliding slab flow in supplementary video 2), which need to be excluded in the determination of the front position as they separate from the main body of the flow. Hence, the front position is determined by ~~excluding~~ ruling out 1% of the particles at the front of the flow~~to minimize the effect of scattered particles from the main flow~~. The front in Fig. 3(a) is

185 calculated as the horizontal distance between the current front position and the initial front position. The gray band in Fig. 3(a) shows the region where a flow front enters the connecting arc zone, below and above which the flow front is on the slope and in the horizontal deposition area, respectively. The evolution of front velocity in Fig. 3(b) is plotted with two constant velocities v_{max}^b and v_{max}^f, which are the theoretical velocities of a sliding rigid block with and without consideration of bed friction, respectively. Referring to Fig. 1, if a rigid block slides down the slope, its path length prior to the connecting arc zone

190   is $l = L/\cos\theta - r\tan\theta - 0.5l_0$ $l = L_0/\cos\theta - r\tan\theta - 0.5l_0$. Its acceleration along the flow direction is $a^b = g(\sin\theta - \mu\cos\theta)$ considering gravity and friction or $a^f = g\sin\theta$ with a frictionless bed, where μ is the bed friction coefficient fixed to 0.5 as listed in Table 1. Given l, a^b, a^f, the theoretical velocities when the block goes to the end of the slope can be calculated as $v^b_{max} = \sqrt{2a^b l}$ and $v^f_{max} = \sqrt{2a^f l}$ with and without consideration of the bed friction, respectively.
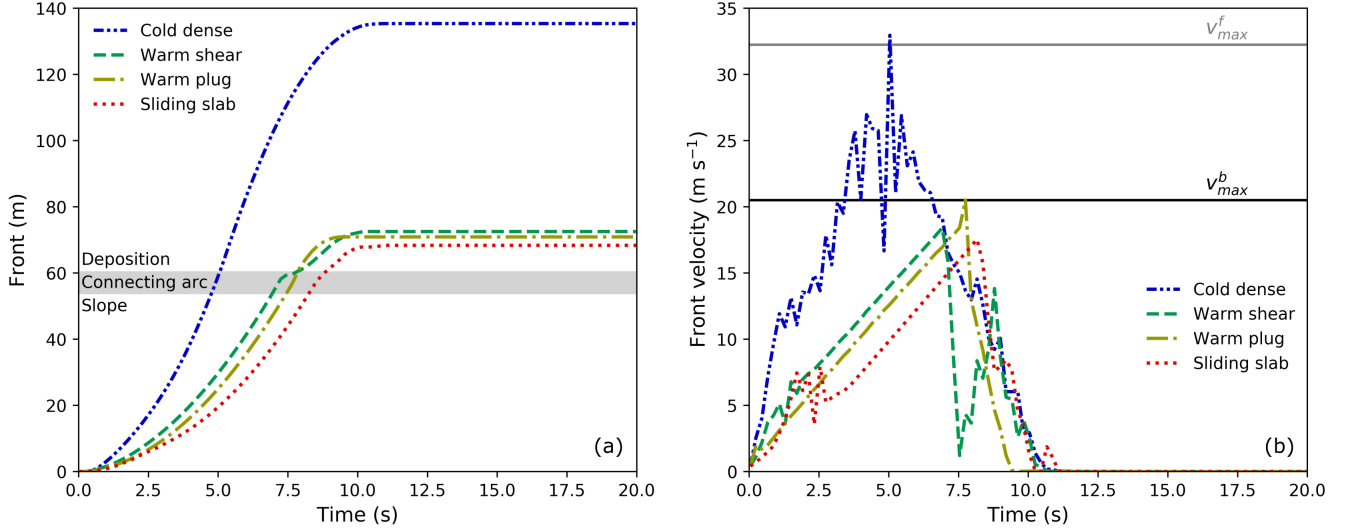
Figure 3. Evolution of (a) front and (b) front velocity of the flows in the four typical regimes (Table 1, Group II).

When the flows are on the slope (front < 53.82 m), the front of the cold dense flow is the fastest, followed by the warm shear

195   and warm plug flows, and the sliding slab is the slowest. Indeed, the front velocity in Fig. 3(b) generally gives a consistent trend. The warm shear and sliding slab flows demonstrate fluctuations at around 1.2 s and 2.2 s in Fig. 3(b), due to the breakage of the snow sample. The tensile strength of the snow in the warm shear flow (9 kPa) is smaller than the sliding slab (21 kPa), leading to the earlier breakage and earlier fluctuations in Fig. 3(b). The fluctuations in the front velocity of the cold dense flow last longer, which might be due to the turbulence and surges as observed in Fig. 2(a). After the flows enter the connecting

200   arc zone (53.82 m < front < 60.25 m), the fronts of the cold dense, warm plug and sliding slab flows evolve smoothly in Fig. 3(a), whilst the front of the warm shear flow is sharply slowed down at the end of the connecting arc zone before it goes to the horizontal deposition zone. In the warm shear flow, discrete granules form a discontinuous flow front. After the scattered granules arrive at the end of the connecting arc zone, they quickly stop, leading to the stagnancy in the increase of the front position until the arrival of continuously incoming granules. Indeed, the warm shear flow in Fig. 3(b) shows the sharp velocity

205   reduction at around 7.5 s, after which the growth of velocity occurs thanks to the incoming flow. A significant drop is also observed from the front velocity of the cold dense flow at around 4.8 s in Fig. 3(b), corresponding well to the moment that the flow front reaches the connecting arc zone in Fig. 3(a). Indeed, this reduction is mainly contributed from the changed slope geometry in addition to the turbulence and surges in the cold dense flow. In Fig. 3(b), the maximum front velocities of the warm shear, warm plug and sliding slab are close to v^b_{max}, whilst the maximum front velocity of the cold dense flow reaches v^f_{max}.

210 This indicates different dominant factors of the maximum flow velocity. The maximum velocity of the flows in warm shear, warm plug and sliding slab regimes is chiefly governed by the frictional behavior between the flow and the bed. In contrast, the maximum velocity of the cold dense flow is mainly controlled by the snow properties, where the low friction and low cohesion facilitate a higher velocity. When the flow fronts enter the deposition zone (front > 60.25 m), all the flows start to slow down gradually. It is noticed that the front velocity of the warm shear flow shows fluctuations from around 7.5 s, which are chiefly

215 because of the discrete nature of the snow granules at the flow front (see supplementary video 1). As the front velocity of the warm shear flow decreases at around 7.5 s, the warm plug flow exceeds the warm shear flow. Nevertheless, the final front of the warm shear flow goes further as it stops later. The final fronts of the four flows show a consistent relation as that obtained when they are on the slope. Before the flows stop, the decelerations of the fronts (slope of velocity in Fig. 3(b)) are similar, which might be governed by bed friction.

220 ### 3.2.2 Evolution of free surface shape and vertical velocity profile

Fig. 4 shows the evolution of free surface and velocity profile of the flows in the different flow regimes. The velocity profile is obtained at $x = 50$ m. The free surface of the cold dense flow in Fig. 4(a) is scaled up 15 times along the bed-normal direction to visualize the fluctuations at the surface. The height of the cold dense flow is much smaller than the initial flow height, since it is highly sheared throughout its flow depth as shown in Fig. 4(e). The velocity profiles in Fig. 4(e) are smooth, indicating

225 the continuous shearing along the flow depth. The shape of the velocity profile in Fig. 4(e) does not change much with time, whilst the flow speed and the shear rate decrease as the flow tends to stop. Generally speaking, the cold dense flow behaves as a fluid or a noncohesive granular flow, in agreement with the characterization by Köhler et al. (2018). The warm shear flow in ~~Figs~~Fig. 4(b) demonstrates a fluctuated free surface because of the formed granules. Correspondingly, its velocity profile shows fluctuations as well. As illustrated in Fig. 4(f), the warm shear flow is fully sheared along the flow depth direction before

230 it stops. Moreover, its flow depth can exceed the initial flow height due to the piling up and accumulation of snow granules. The shear behavior and the piling up feature are indeed consistent with the identified warm shear regime by Köhler et al. (2018). Nevertheless, instead of a noncohesive granular flow characterized by Köhler et al. (2018), the flow in our MPM modeling does have cohesion (see Table 2), which helps the formation of the granules. The warm plug flow remains a block and is seldom sheared when it slides on the slope. Upon its arrival at the connecting arc zone, significant shearing occurs due to the changed

235 shape of the connecting arc zone. As shown in Figs ~~.~~ 4(c) ~~&~~and (g), the front of the warm plug flow is notably sheared at t = 8.0 s, the flow body is only sheared at the bottom layer at t = 8.3 s, and the flow tail is seldomly sheared at t = 8.8 s. The sliding slab in Fig. 4(d) shows the sliding down of the slabs from t = 9.0 s to 9.2 s and the accumulated slabs in the connecting arc and deposition zones at t = 10.5 s. As there are particles stopping on the slope, the tail of the free surface collapses onto the slope. The shearing behavior inside the slabs is extremely limited as shown in Fig. 4(h). Both the warm plug and the sliding

240 slab behave as solid-like objects, while the snow of the sliding slab flow is more brittle and produces slab fractures.
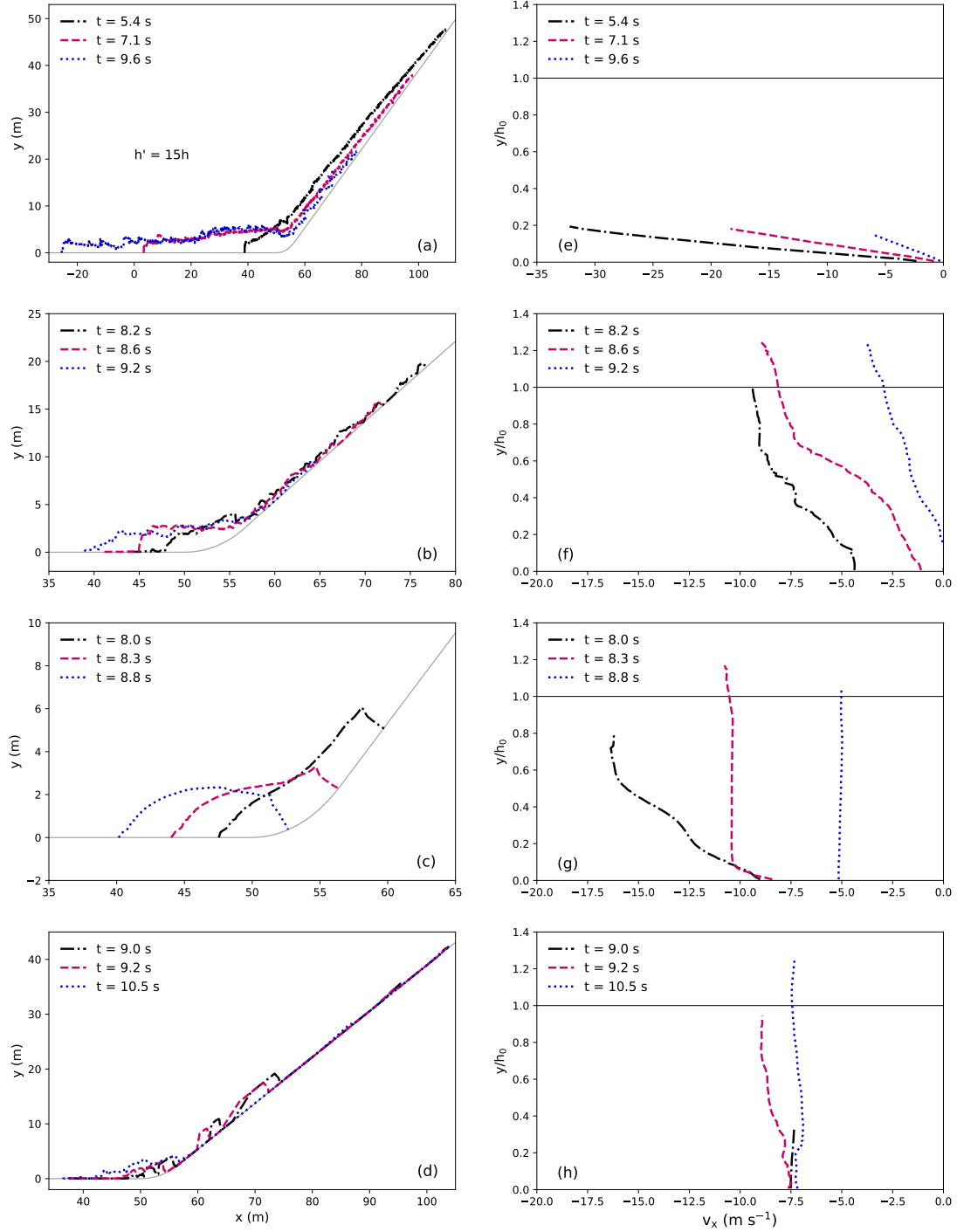
Figure 4. Evolution of free surface shape (left column) and velocity profile at ~~x~~ x = 50 m (right column) for the flows in the different regimes (Table 1, Group II). (a)&(e) cold dense; (b)&(f) warm shear; (c)&(g) warm plug; (d)&(h) sliding slab. The free surface of the cold dense flow in (a) is scaled up 15 times along the bed normal direction for better visualization.

11

3.3 Effect of slope angle and path length on flow dynamics

3.3.1 Maximum velocity and deposition height

Figs. 5 and 6 demonstrate the evolution of the maximum avalanche velocity on the slope v_{max} with the normalized avalanche deposit height h_d/h_0, under the effects of the slope angle θ and the horizontal length L_0 (reflecting the path length), respec-
245 tively. The deposit height h_d is defined as the maximum avalanche height along the bed normal direction after snow avalanches stop. The maximum velocity of snow avalanches is usually obtained before their arrival at the deposition zone. To analyze our MPM data with theoretical predictions, the maximum velocity v_{max} in Figs. 5 and 6 is determined when the flow is on the slope. For all the simulated groups in Figs 5 and 6, a similar trend is observed, with three zones indicating different flow characteristics and flow regimes. Zone A shows a maximum velocity which tends to be negatively correlated with the deposit
250 height. A typical flow regime is the cold dense regime, in which a higher maximum flow velocity leads to a longer run-out distance and a smaller deposit height. The black data in Zone A reflects small snow friction and cohesion, which agrees with the snow properties of the cold dense flow. Zone B has a deposit height close to the initial height of the snow sample. This characteristic is normally captured from the warm plug and sliding slab flow regimes. Note that, in addition to the typical case in the sliding slab regime in Fig. 4(d) which demonstrates accumulated snow in the deposition zone, there are other cases with
255 slabs sliding down the slope and stopping in the deposition zone without piling up and snow accumulation. These cases in the sliding slab regime give a final deposit height close to the initial flow height. The high snow friction and cohesion reflected by the light color in Zone B indeed indicate the snow properties of the warm plug and sliding slab flows. In Zone C, the deposit height is notably larger than the initial height. In this case, representative flow regimes are the warm shear flow and the sliding slab flow, where the accumulation of snow can be significant after the flows deposit. It is found that the flowing and deposition
260 behaviors of snow avalanches are primarily controlled by the snow friction and snow cohesion (M and β), as we observe the clear transition of colors denoting $M\beta$ in the different zones in Figs. 5 and 6. The scattered colors of some points, such as the dark points in Zone C, indicate the additional effects of snow brittleness (reflected by ξ) and snow compressive strength (p_0).

Slope angle is a key factor in evaluating the trigger, flow and deposition of snow avalanches (Gaume, 2012; Sovilla et al., 2010). Fig. 5 shows the positive correlation between the slope angle θ and the maximum velocity on the slope v_{max}. When θ is
265 varied with a fixed L_0 (see Fig. 1), the drop height H_0 is increased accordingly, which gives a larger initial potential energy of the flow and consequently a higher v_{max}. The effect of increased path length reflected by L_0 is similar to the outcome of the growth of θ, as shown in Fig. 6. It is interesting to observe the similar trend for the different groups of simulations with varying θ and L_0, which hints an analogous physical rule behind the trend. Indeed, a unified relation can be obtained as shown in Fig. 7, by scaling v_{max} and h_d as follows

$$270 \quad v_{max}^* = \frac{v_{max} - v_{max}^b[1 - e^{-M(1+\beta)/\kappa_1}]}{v_{max}^f} \tag{6}$$

$$h^* = \frac{h_d}{h_0}[1 - e^{-M(1+\beta)\kappa_2/l}] \tag{7}$$

12
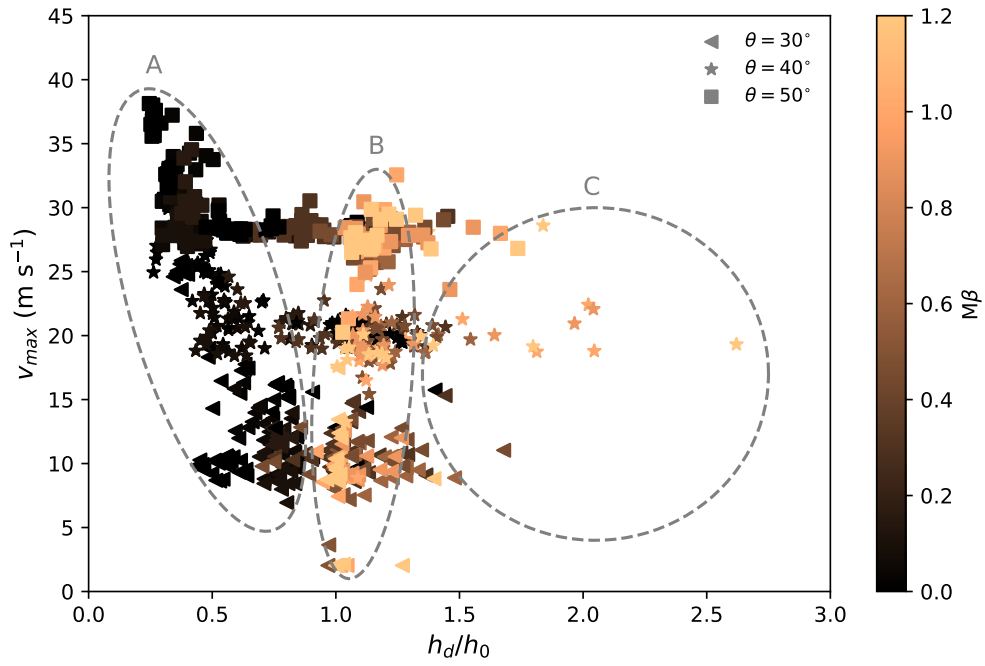
Figure 5. Evolution of the maximum velocity with the normalized deposit height for varying slope angles θ.
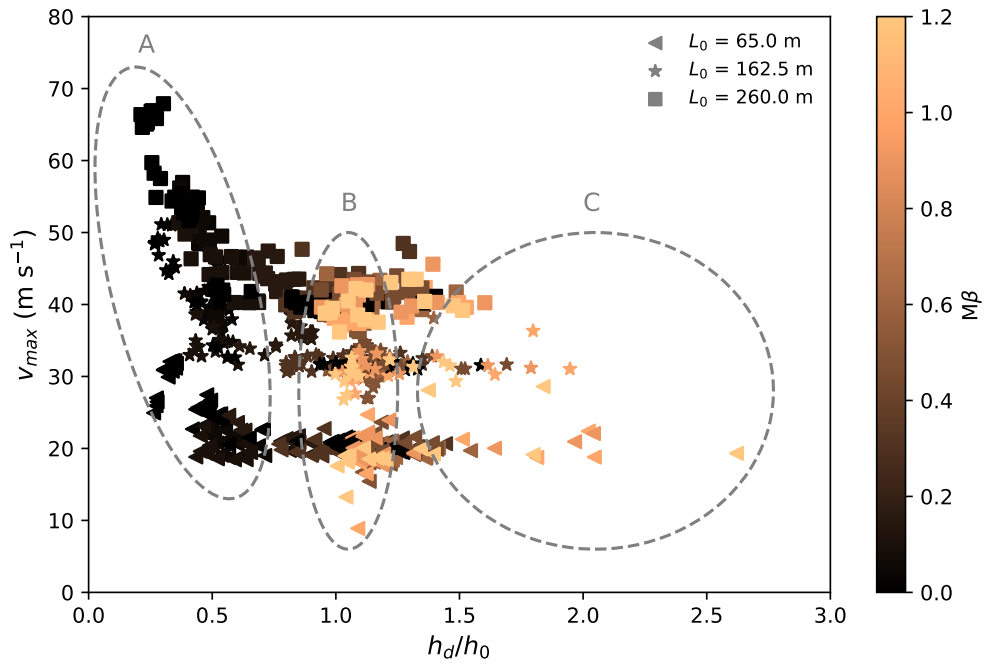

Figure 6. Evolution of the maximum velocity with the normalized deposit height for different horizontal lengths L L_0.
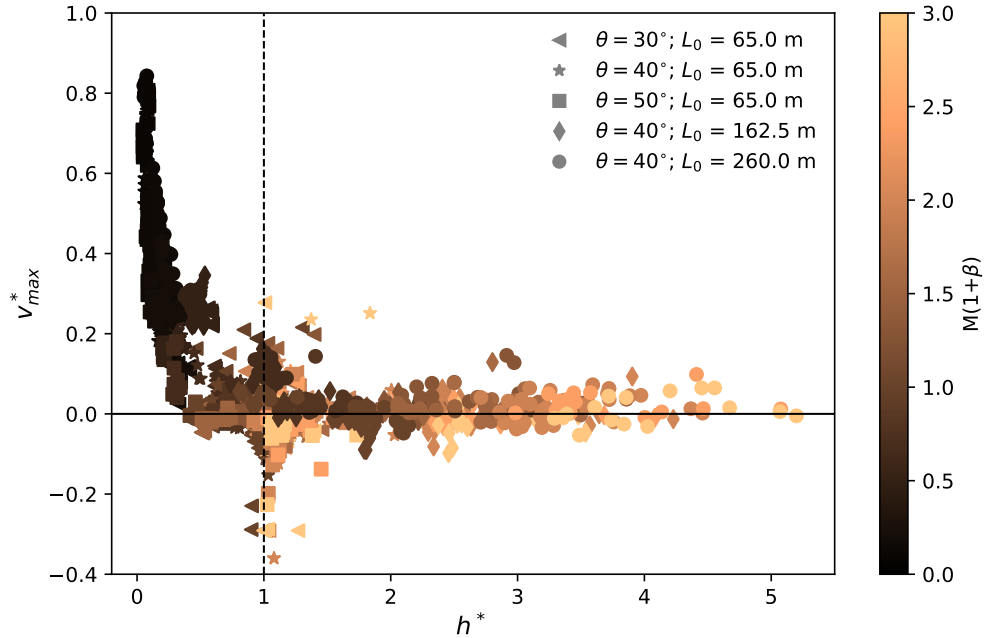
Figure 7. Unified relation between the scaled maximum velocity and the scaled deposit height.

The normalization of v_{max} takes into account v_{max}^b and v_{max}^f, which are the theoretical predictions with a frictional bed and a frictionless bed, respectively. The consideration of v_{max}^b and v_{max}^f reflects the influence of bed friction, slope angle and path

275 length. In addition, the effect of snow friction (M) and cohesion (β) ~~are~~ is also considered. The deposit height h_d is scaled with the initial height of the snow slab, the snow properties, and the path length. Note two constant coefficients κ_1 and κ_2 are used to account for other possible factors including snow compressive strength and brittleness, where κ_1 is dimensionless and κ_2 has a ~~unit of meter~~ dimension of length. In this study, κ_1 and κ_2 are 0.2 and 200 m, respectively. According to Eq. (6), when the friction M and cohesion β of snow are high, the numerator is close to $v_{max} - v_{max}^b$, and a zero numerator indicates a maximum

280 velocity close to the theoretical prediction considering a rigid block sliding on a frictional bed. As shown in Fig. 7, the data around the zero line hint that the maximum velocity of the flows are chiefly controlled by the friction between the flow and the bed. On the other hand, when M and β tend to zero, v_{max}^* approaches v_{max}/v_{max}^f in Eq. (6), reflecting how close is the maximum flow velocity to the theoretical prediction with a rigid block sliding on a frictionless bed. Correspondingly, the cases with small M and β in Fig. 7 reflect a maximum flow velocity primarily governed by snow properties, instead of the frictional

285 behavior between the flow and the bed. A representative case is the cold dense flow in Fig. 3(b), where its maximum velocity is close to v_{max}^f as the flow is highly sheared. Furthermore, data below the zero line is observed in Fig. 7, corresponding to the cases where the snow box either stays on the slope with limited displacement or slides down the slope with a velocity sometimes decreased (i.e. not a constant acceleration as assumed in the calculation of v_{max}^b).

14

3.3.2 Maximum velocity and α

The runout angle α is defined as $\alpha = \arctan(H/L)$. H and L are total vertical drop and total horizontal reach, respectively, determined based on the top point of the release zone and the front of the final deposit (Lied and Bakkehøi, 1980). Figs. 8 and 9 show the relation between v_{max} and α, including MPM data and real-measurement data collected from McClung and Gauer (2018). For the five groups of MPM simulations varying the slope angle θ and horizontal length L_0, all of them largely follow a two-stage relation between v_{max} and α: an initially decreasing v_{max} and a subsequently constant v_{max} with the increase of α. As demonstrated in Figs. 8 and 9, the first stage mainly consists of cases with low friction and cohesion, whilst the second stage is chiefly composed of cases with high friction and cohesion. At the first stage, a higher v_{max} leads to a longer runout distance and thus a smaller α. This indicates the dominant effect of v_{max} in controlling the runout distance, which might be due to the positive correlation between the velocity and the kinetic energy of a snow avalanche. Indeed, it has been recognized that the runout distance is tightly related to the kinetic energy of the flow upon its arrival at the deposition zone (Sovilla et al., 2006). Obviously, the dominance of v_{max} disappears at the second stage, as a similar v_{max} gives a notably different α. The runout distance at this stage is mainly affected by the deposition behavior, instead of the flowing behavior. For example, assuming a warm plug flow and a warm shear flow sharing an identical v_{max} before they reach the deposition zone, their runout distances can differ much, since the warm plug flow may stop abruptly whilst the warm shear flow may gradually become steady and have a relatively longer runout distance.

From Figs. 8 and 9, the effects of θ and L_0 on v_{max} are similar, as both of them have a positive correlation with v_{max}. In addition, the slope angle θ also influences the maximum runout angle as shown in Fig. 8. The larger the slope angle, the larger the maximum runout angle. This is due to the definition of the runout angle α, which gives a maximum runout angle close to the slope angle θ. The maximum runout angle is reached when a flow stops on the slope with the modeled configuration. With $\theta = 30°$, several flows stay on the slope and have $\alpha \approx \theta$. All the flows with $\theta = 40°$ and $50°$ go to the connecting arc and deposition zones, giving $\alpha < \theta$. Note that the runout angle α has been correlated to the mean slope angle β in exploring the runout distance of snow avalanches (Lied and Bakkehøi, 1980; Barbolini et al., 2000; Delparte et al., 2008). As ideal slopes are adopted (see Fig. 1) here, the mean slope angle β is close to the slope angle θ. Indeed, the positive correlation between the maximum runout angle and the slope angle in Fig. 8 agrees with the $\alpha - \beta$ model (Lied and Bakkehøi, 1980). The MPM results in Figs. 8 and 9 generally fall onto the range of the real-measurement data from McClung and Gauer (2018). In particular, the lower-bound of v_{max} from the real measurements is recovered with the MPM simulation. Note the case with $v_{max} = 70$ m/s serving as the upper-bound of the field data was a powder snow avalanche, whose behavior differs much from the simulated dense snow avalanches. In addition, the path length of the upper-bound case is significantly higher than the adopted ones in the MPM simulations (McClung and Gauer, 2018). This upper-bound case can indeed be captured with our MPM modeling by varying the model setup, but is not the focus here. It was reported by McClung and Gauer (2018) that the runout angle has a negative correlation with the maximum front velocity, but with wide scatter as observed from the blue dots in Fig. 8 or Fig. 9. According to our sensitivity study, the scatter might be a result of different terrain conditions (e.g. slope angle),

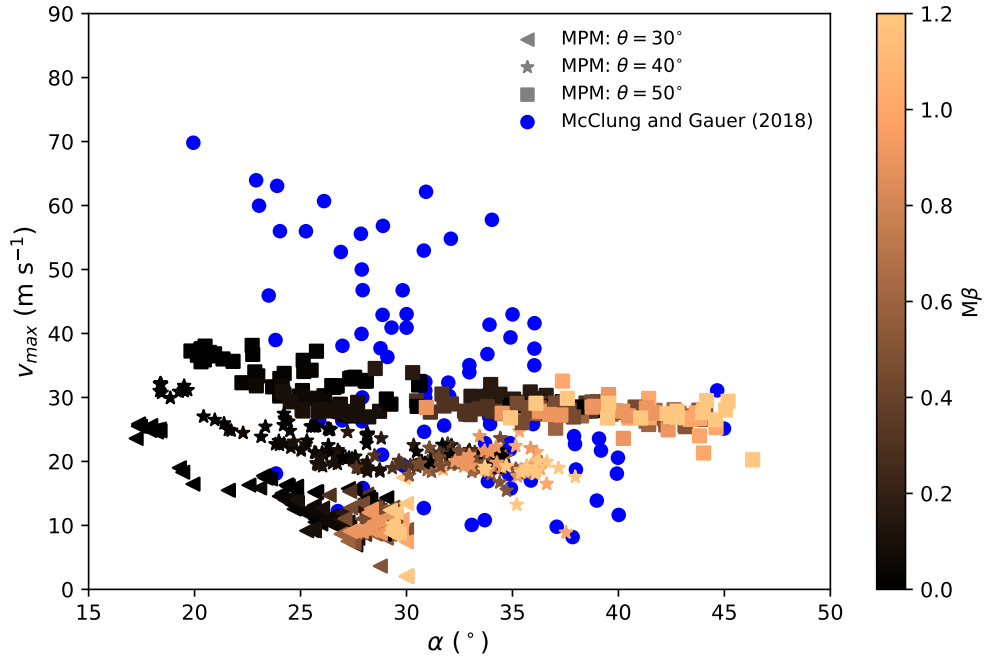**Figure 8.** Evolution of the maximum velocity with α for varying slope angles θ.

release positions (e.g. path length), and snow properties. In addition, some data might be on the plateau stage where the runout distance is governed by the deposition behavior instead of the maximum front velocity.

325   Fig. 10 demonstrates a unified trend with the dimensionless velocity v^*_{max} in Eq. (6) and α^* as follows

$$\alpha^* = \frac{\alpha}{\alpha^b} \tag{8}$$

where α^b is calculated by assuming a sliding rigid block. Referring to Fig. 1, the velocity of the block increases from 0 to $\sqrt{2a^bl}$ as it slides down from the upstream to the end of the frictional slope. With an assumption that the velocity of the block does not change before and after it goes across the connecting arc zone, its runout distance on the deposition zone can be calculated, with

330   an initial velocity of $\sqrt{2a^bl}$, a constant acceleration of $-\mu g$, and a final velocity of 0. α^b can then be derived as $\alpha^b = \arctan\mu$. It is interesting to obtain α^b solely dependent on the bed friction coefficient μ. The scaled runout angle $\alpha^* = 1$ means a runout distance fully consistent with the prediction using the sliding rigid block theory, whilst $\alpha^* < 1$ and $\alpha^* > 1$ denote a runout distance which is longer and shorter than the predicted one with the sliding rigid block theory, respectively. Indeed, the data with $\alpha^* < 1$ in Fig. 10 generally have low friction and cohesion, which reasonably produce the longer runout distances. On the

335   contrary, the cases with $\alpha^* > 1$ are typically more frictional and cohesive, leading to the shorter runout distances. ~~As discussed in Fig. 7,~~ Note that the data close to the zero line in Fig. 10 ~~indicate their~~ correspond to the cases at the plateau stage in Figs 8 and 9. As discussed in Fig. 7, when the friction M and cohesion β are high, a zero v^*_{max} comes from a maximum velocity v_{max} ~~controlled~~ that approaches the theoretical prediction v^b_{max} with consideration of a rigid block sliding on a frictional bed,
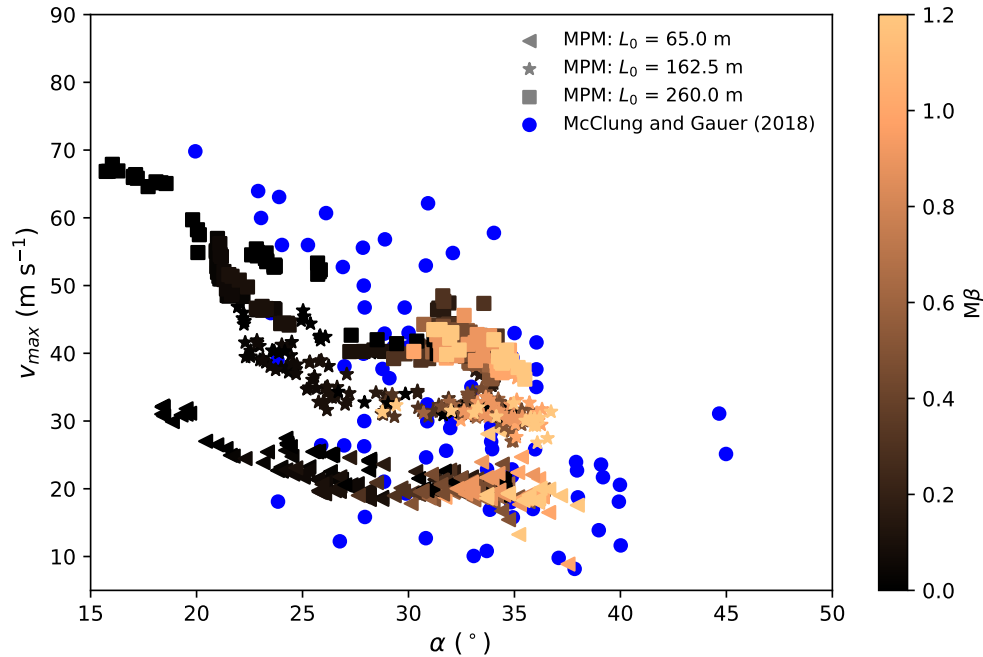
16

Figure 9. Evolution of the maximum velocity with α for different horizontal lengths ~~L~~L_0.

indicating the maximum velocity v_{max} is dominated by the frictional behavior between the flow and the bed~~, whilst~~. On the
340   other hand, the v_{max} of the cases far above and below the zero line ~~are~~ in Fig. 10 is governed by the snow properties.

4   Snow avalanches on irregular terrains

~~To calibrate and benchmark our MPM modeling~~ To testify the capability of the MPM modeling in capturing key dynamic
features (i.e. front velocity and position) of snow avalanches, five reported real avalanches with different complex terrains are
simulated. All the cases are modelled in 2D, neglecting the variation along the flow width direction. The adopted geometry of
345   the terrains is borrowed from the literatures. As no detailed snow properties of the avalanches were measured and reported,
the applied snow properties in MPM refer to the description of the snow type and snow condition. In particular, three of the
avalanches mainly consisted of dry, loose and new snow, whilst the other two were chiefly composed of wind packed and settled
old snow. Correspondingly, two groups of snow properties are adopted as summarized in Table 3. Based on the determined
snow densities (150 kg/m^{-3} for new snow and 250 kg/m^{-3} for old snow), the Young's modulus and tensile strength can be
350   estimated using the relations from Gaume (2012) and Scapozza (2004). The friction of the slope is calibrated according to
the existing data of the real avalanches. Figs ~~Figs.~~ 11-15 show the MPM simulation results in comparison with the reported
data from the literatures. Particularly, the evolution of the scaled front velocity is examined along the flow path (Gauer, 2014).
The front velocity from the field was obtained by means of Doppler radar devices and photo analyses. Different measurement
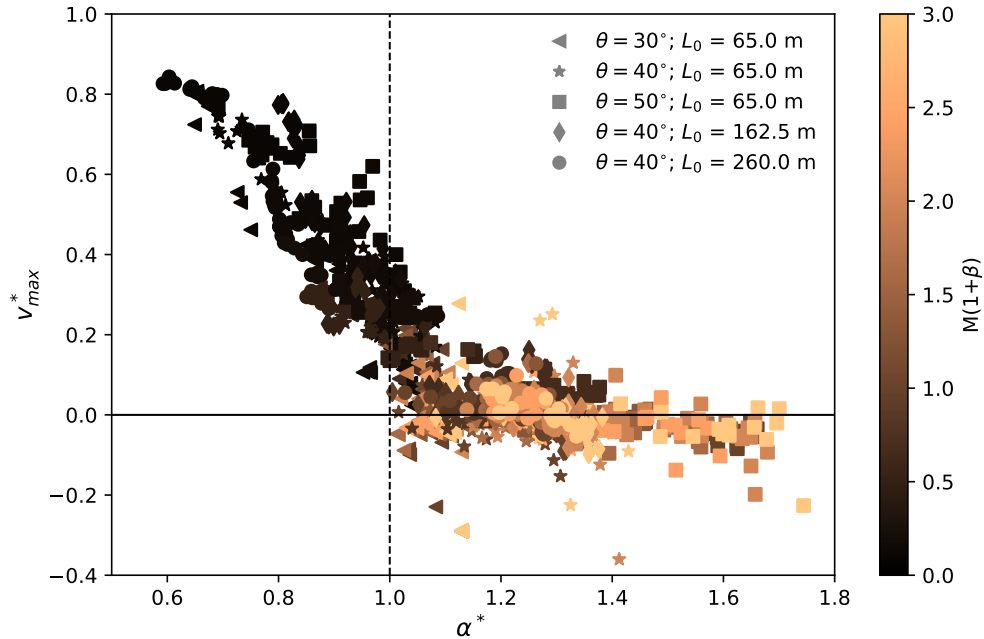
Figure 10. Unified relation between the scaled maximum velocity and the scaled α.

approaches may give different velocities, but are generally consistent with one another (Rammer et al., 2007). The comparison
355 basis between velocities from numerical modeling and real measurements needs to be carefully checked, as it is sometimes
questionable (Fischer et al., 2014; Rauter and Köhler, 2020). For example, depth-averaged velocities from numerical modeling
cannot be directly compared to peak intensity velocities from Droppler radar measurements (Rauter and Köhler, 2020). In Figs
11-15, the front velocity from MPM is determined as the approach velocity (Rauter and Köhler, 2020), which is calculated from
the evolution of the front position with time and is assumed to be comparable with the data from the different measurement
360 techniques. Note that this approach velocity has a different definition from the velocity of the particles at the front of a flow,
although their values are almost identical in our simulations. The geometry of the terrain is denoted by the gray dash curves in
Figs -11-15, where the coordinates x and y are normalized with the vertical drop height HH_0. The red bands in Figs -11-14
denote measurement error.

Case I and II in Figs -11 and 12 are two avalanches successively released at the north-west flank of the Weissfluh-Northridge
365 (Gubler et al., 1986; Gauer, 2014), whose velocity was measured with continuous wave (CW) Doppler-radar. The snow forming
the first avalanche was dry mostly loose new snow, which produced a powder cloud. In comparison, the second avalanche
consisted of wind packed snow, which led to blocky slab-type release. It is noticed that the consistency between the MPM
results and the measured data is better for the second avalanche in Fig. 12. The underestimated maximum front velocity in Fig.
11 might be due to the challenge of capturing the powder could cloud of the first avalanche with MPM. The front velocity of
370 a powder snow avalanche is normally obtained from the frontal dilute part, whose velocity can be higher than the dense core

Table 3. ~~Calibrated~~Adopted parameters ~~for~~ in the five MPM simulations of snow avalanches on real terrains.

		Case I	Case II	Case III	Case IV	Case V
Snow	Density ρ (kg/m^{-3})	150	250	150	250	150
	Young's modulus E (MPa)	0.47	6.45	0.47	6.45	0.47
	Poisson's ratio ν	0.3	0.3	0.3	0.3	0.3
	Friction coefficient M	0.8	0.8	0.8	0.8	0.8
	Tension/compression ratio β	0.1	0.2	0.1	0.2	0.1
	Hardening factor ξ	0.5	0.5	0.5	0.5	0.5
	Initial consolidation pressure p_0^{ini} (kPa)	10	20	10	20	10
	Initial tensile strength βp_0^{ini} (kPa)	1	4	1	4	1
Slope	Bed friction coefficient μ^*	0.46	0.46	0.63	0.51	0.46
Simulation control	Mesh size (m)	0.05	0.05	0.05	0.05	0.05
	Time step (s)	2.3×10^{-4}	2.3×10^{-4}	2.3×10^{-4}	2.3×10^{-4}	2.3×10^{-4}
	Frame rate (FPS)	24	24	24	24	24

*Calibrated parameter.
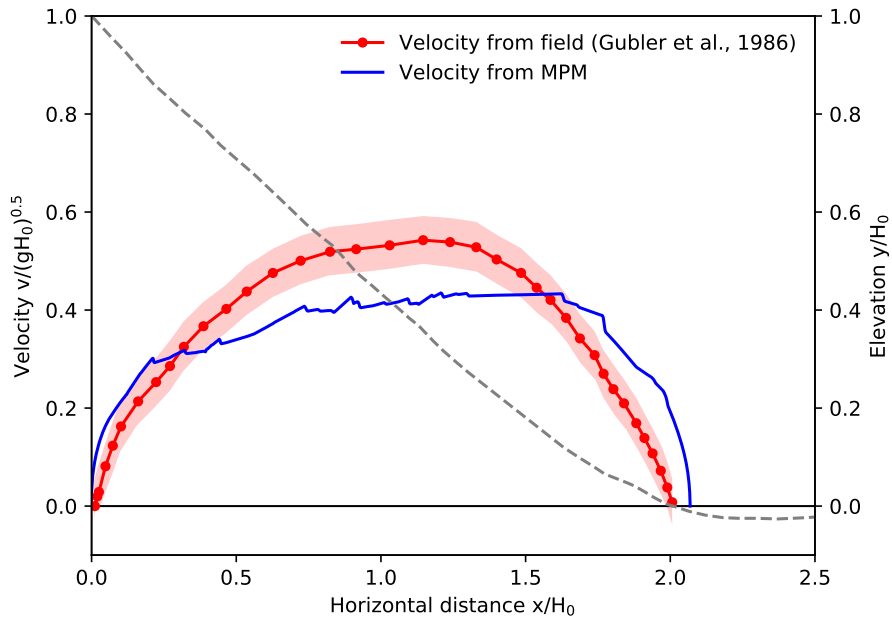
Figure 11. Front velocity distribution along the flow path for Case I: Weissfluh-Northridge 1982-03-12 a1 (Davos, Switzerland). Drop height $H_0 = 236$ m.

of the avalanche (Sovilla et al., 2015). In addition, the neglection of entrainment in the simplified MPM simulation may also contribute to the discrepancy in Fig. 11. It is suspected that the first release induced much more entrainment than the second one, considering the availability of the snow to be entrained.
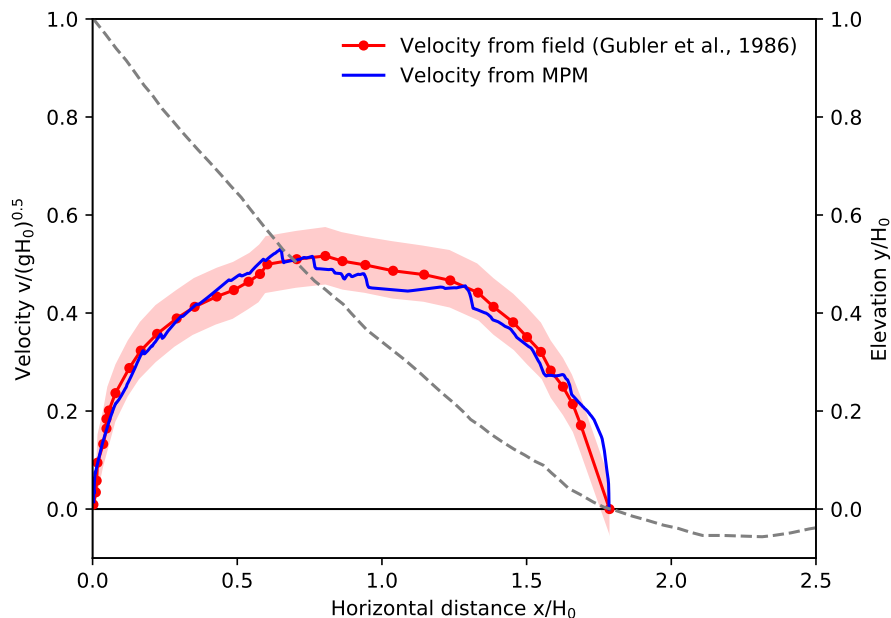

Figure 12. Front velocity distribution along the flow path for Case II: Weissfluh-Northridge 1982-03-12 a2 (Davos, Switzerland). Drop height $H_0 = 177$ m.

Fig. 13 shows the avalanche of Case III, happened after strong snowfall (Gauer, 2014). There were no field observations due to the stormy weather. The velocity was measured by a pulsed Doppler-radar. The snow was conjectured to be dry or only slightly moist. The adopted snow properties in the MPM modeling refer to that of new snow, which are assumed to be identical to the snow in Case I as listed in Table 3. Fig. 13 illustrates reasonable agreement between the MPM and the measured data, in terms of both the final front position and the maximum front velocity. During the flowing process, MPM tends to underestimate the front velocity, which might be related to the dry nature of the snow as discussed in Case I (Fig. 11). Compared with Cases I and II, the front velocity evolution of Case III is more fluctuated, as the terrain is more irregular.

Case IV in Fig. 14 is a snow avalanche composed of snow cornice at the release position and settled old snow in the track (Gauer, 2014). The consistency between the MPM data and the estimated velocity from a series of timed photographs (Gauer, 2014) is satisfactory, except for the overestimated velocity at the beginning of the flow. The overestimated front velocity from MPM is tightly related to the abruptly steepened slope at ~~x/H~~ $x/H_0 \approx 0.2$. The increase of front velocity in reality was not as sharp as the MPM result, which might be due to the effect of more entrainment especially at the steep part of the slope. Indeed, it was reported that the maximum velocity of a simulated snow avalanche without entrainment is higher than that with entrainment, given the same runout distance (Sovilla and Bartelt, 2002; Sovilla et al., 2007). Moreover, the measurement data
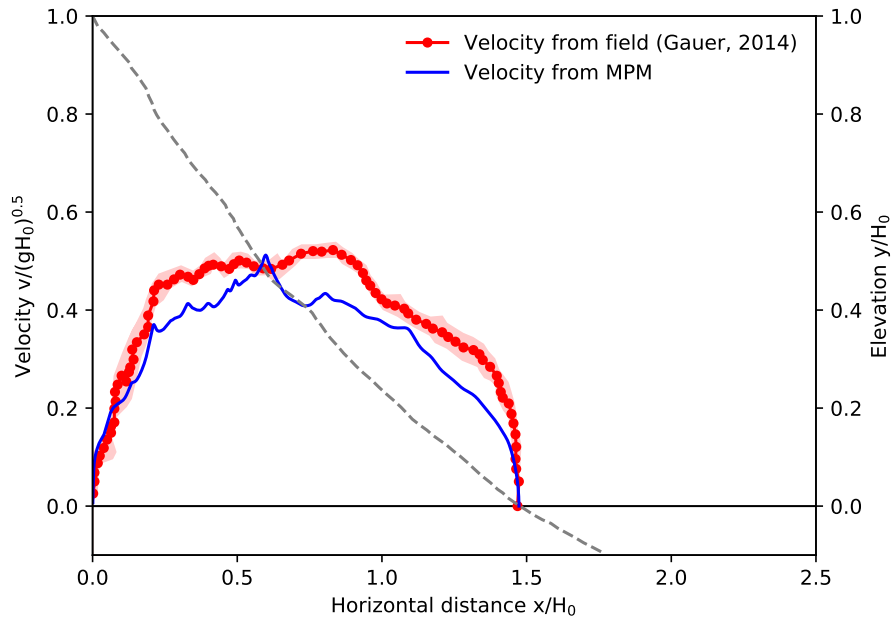
Figure 13. Front velocity distribution along the flow path for Case III: Himmelegg 1990-02-14 (Alberg, Austria). Drop height $H_0 = 352$ m.
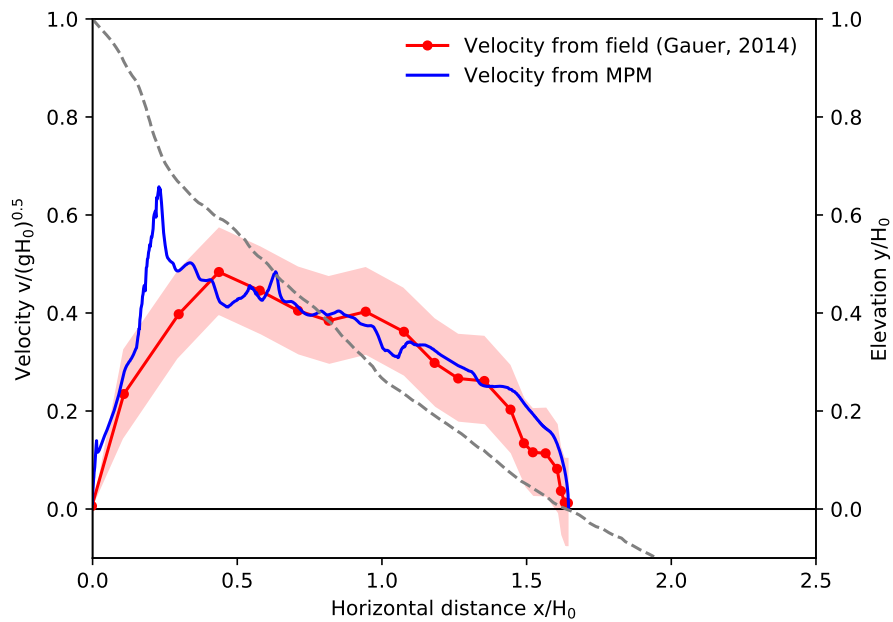

Figure 14. Front velocity distribution along the flow path for Case IV: Ryggfonn 2006-05-02 (Stryn, Norway). Drop height $H_0 = 303$ m.
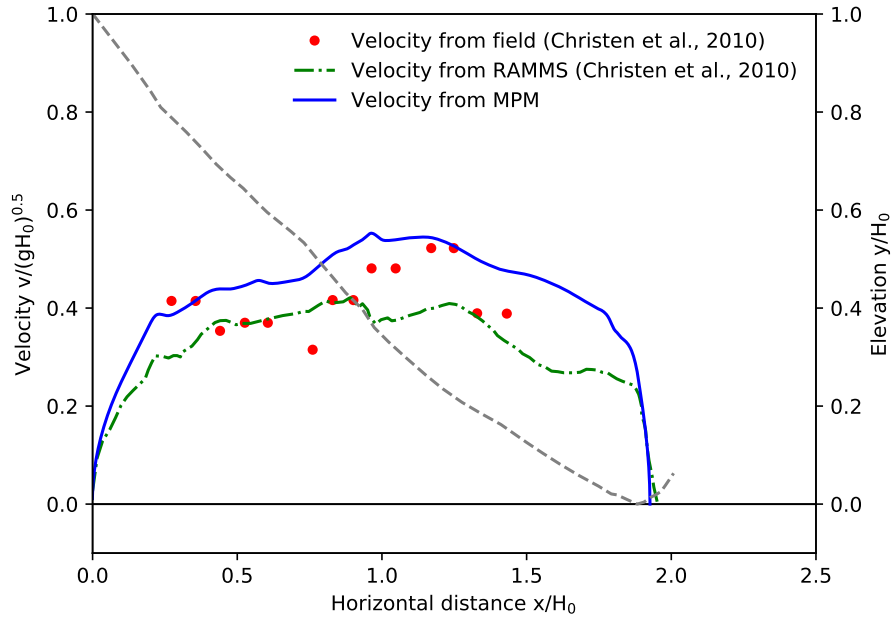
Figure 15. Front velocity distribution along the flow path for Case V: VdlS 2003-01-31 (Sion, Switzerland). Drop height $H_0 = 1246$ m.

are based on photo series with intervals of 1 s, whilst the time gaps of the MPM data are 1/24 s. The maximum front velocity in reality might be lost within the 1 s interval of the measurement.

Fig. 15 demonstrates the data of Case V, including that from real measurement and RAMMS simulation (Christen et al., 2010) as well as our MPM modeling. The front velocity from the field was calculated from timed photographs. The dry snow avalanche in Case V was artificially triggered, and the development of powder part was reported (Christen et al., 2010). To be consistent, the adopted properties for the dry snow in Cases I and III are used for Case V. As shown in Fig. 15, both the RAMMS and MPM results show reasonable consistency with the real-measurement data. The calculated final front positions from RAMMS and MPM are similar, whilst the maximum front velocity is underestimated and overestimated by RAMMS and MPM, respectively. As discussed in Case IV, the MPM modeling does not take entrainment into account, which might be the reason of the overestimated front velocity.

5 Conclusions and discussion

This study explores the dynamics of snow avalanches with the Material Point Method (MPM) and an elastoplastic constitutive model. By virtue of the capability of the MPM in simulating processes with large deformations, fractures, collisions and coexistence of solid- and fluid-like behaviors, a wide range of distinct snow avalanches with diverse flow behaviors has been investigated. The reported four flow regimes for dense snow avalanches from real observations have all been captured from our MPM simulations, including cold shear, warm shear, warm plug and slab sliding regimes. Moreover, in transition from cold

shear to warm shear flow regimes, flows with surges and small granules are observed. The evolution of the avalanche front, the free surface shape, and the vertical velocity profile shows distinct characteristics for the different flow regimes, underpinning the identification of flow regime. In addition to the flow surface and the shear behavior presented in this study, other features of the flow may also be used to pinpoint the flow regimes, such as snow temperature and liquid water content (Köhler et al., 2018). Although they are not explicitly taken into account in this study, the changing snow properties in our MPM modeling are capable of capturing the characteristics of the different regimes. Furthermore, distinct stopping mechanisms and maximum velocities were reported for the four regimes (Köhler et al., 2018). For example, the cold dense regime was identified by starving stopping mechanism, where the flow deposits and stops firstly from its tail then to its front. And the velocity of the cold dense regime was reported to be smaller than 30 m/s. It is noticed that the simulated flow with MPM does not fully follow these descriptions, which might be due to the idealized MPM setup and different terrain conditions.

We have systematically examined the effects of snow properties, slope angle, and path length on the flow and deposition behaviors of snow avalanches, including the maximum flow velocity on the slope, the α runout angle and the avalanche deposit height. It is found that snow friction and cohesion are closely related to the behaviors behavior of snow avalanches. Low snow friction and cohesion give fluid-like behaviors behavior and highly sheared flows, while high snow friction and cohesion lead to solid-like flows flow with limited shearing. Both slope angle and path length have a positive correlation with the maximum flow velocity on the slope, whilst their effects on the deposit height are trivial. Furthermore, unified trends have been obtained with normalization of the maximum flow velocity, the deposit height and the α runout angle, revealing analogous physical rules under the different conditions. Key controlling factors of v_{max} has been identified, including the friction between the bed and the flow, the geometry of the slope, as well as the snow properties. Depending on snow properties, the α runout angle is either controlled by the flow behavior of a snow avalanche before its arrival at the deposition zone, or governed by its deposition behavior. It should be noted that a wide range of material parameters has been adopted for the sensitivity study. The combination of extreme flow properties leading to very high velocity might not be realistic for snow avalanches. The material parameters need to be carefully calibrated for investigation of real snow avalanches.

The MPM model has been benchmarked and calibrated with modeling has been calibrated and tested through simulations of real snow avalanches on irregular terrains. The calculated avalanche front position and velocity from MPM show reasonable agreement with the measurement data from literatures literature. The behavior of dense snow avalanches has been well recovered by MPM. Discrepancy was observed particularly for avalanches which developed a powder cloud above the dense core, as the powder cloud has not been modeled here.

The presented research focus focuses on examining the flow regimes and flow dynamics of snow avalanches with idealized conditions, which is a preliminary study serving as the basis for investigating more realistic and complex snow avalanches. The 2D ideal slope with a constant inclination could be further changed to other shapes to be more realistic, such as parabolic track. Although the 2D setups were used to efficiently conduct the systematic study including more than 1000 cases, it is fully possible to explore interesting cases with 3D MPM simulations (Gaume et al., 2019). Future studies will take into account real topography in 3D and recover the natural boundary conditions of snow avalanches. In addition, a new framework will need to be developed for investigating snow avalanches with a powder cloud, by considering a new constitutive law for the cloud and

its interaction with both the dense core of snow avalanches and the air around the cloud (e.g. air friction). To further consider entrainment, the snow cover could be explicitly simulated with our model. This would however significantly increase the computational time. Alternatively, one could add a mass flux rate term to the mass balance equation, which considers the snow cover as a rigid boundary and estimates the entrained mass based on empirical and theoretical relations (Naaim et al., 2004; Issler and Pérez, 2011). Meanwhile, the momentum conservation needs to be adjusted to account for the momentum change of snow avalanches due to entrainment. Despite the assumptions and idealization applied in this study, it is demonstrated that the MPM model provides a promising pathway towards systematic and quantitative investigations on snow avalanche dynamics and flow regime transitions under the effects of snow mechanical properties and terrain geometries, which can improve our understanding of wet snow avalanches and offer analysis for avalanche dynamics with the influence of climate change.

Appendix A: Energy evolution of the flows in the four typical flow regimes

The constitutive model adopted in this study perfectly satisfies the second law of thermodynamics. Following the derivation in Gaume et al. (2018a), proving energy does not increase is equivalent to proving the plastic dissipation rate $\dot{w}^P(\boldsymbol{X},t)$ is non-negative. $\dot{w}^P$ can be computed as

$$\dot{w}^P = -\boldsymbol{\tau} : \frac{1}{2}(\mathcal{L}_v \boldsymbol{b}^E)(\boldsymbol{b}^E)^{-1} \tag{A1}$$

where $\boldsymbol{\tau}$ is the Kirchhoff stress tensor, $\mathcal{L}_v$ is the Lie derivative, and $\boldsymbol{b}^E$ is the elastic right Cauchy-Green strain tensor. Since we use an associative flow rule, $\mathcal{L}_v \boldsymbol{b}^E = -2\dot{\gamma}\frac{\partial y}{\partial \boldsymbol{\tau}}\boldsymbol{b}^E$ (see Equation 10 in Gaume et al. (2018a)), $\dot{w}^P$ can be expressed as

$$\dot{w}^P = \boldsymbol{\tau} : \dot{\gamma}\frac{\partial y}{\partial \boldsymbol{\tau}} = \dot{\gamma}\hat{\boldsymbol{\tau}} \cdot \frac{\partial y}{\partial \hat{\boldsymbol{\tau}}} \tag{A2}$$

Recall Equation 11 in Gaume et al. (2018a) that $\dot{\gamma} \geq 0$. Furthermore, $\hat{\boldsymbol{\tau}} \cdot \frac{\partial y}{\partial \hat{\boldsymbol{\tau}}} \geq 0$ because the yield surface is a convex function of $\hat{\boldsymbol{\tau}}$ which includes the origin. Therefore $\dot{w}^P \geq 0$. Notes this result holds for any isotropic plasticity model that has a convex yield function and an associative flow rule.

The evolution of kinetic and potential energy of the flows in the four typical flow regimes (i.e. cold dense, warm shear, warm plug, sliding slab) is demonstrated in Fig. A1. As expected, the potential energy of the flows initially decreases as the flows move down from the slope, and then becomes steady after the flows stop. The kinetic energy of the flows firstly increases and then reduces until it vanishes. It is noticed that the kinetic energy of the sliding slab shows fluctuations in the deceleration phase, due to the interactions between the separating slabs in the flow after they reach the connecting arc zone (see supplementary video 1).

Fig. A2 shows the dissipated energy of the flows in the four cases. The dissipated energy increases before it reaches the final steady state. The growth rate of the dissipated energy varies for the different flows as they have distinct flow behaviors. Nevertheless, the final energy dissipation does not show much difference for the different flows. This is because of the identical initial potential energy and the similar final potential energy of the flows.
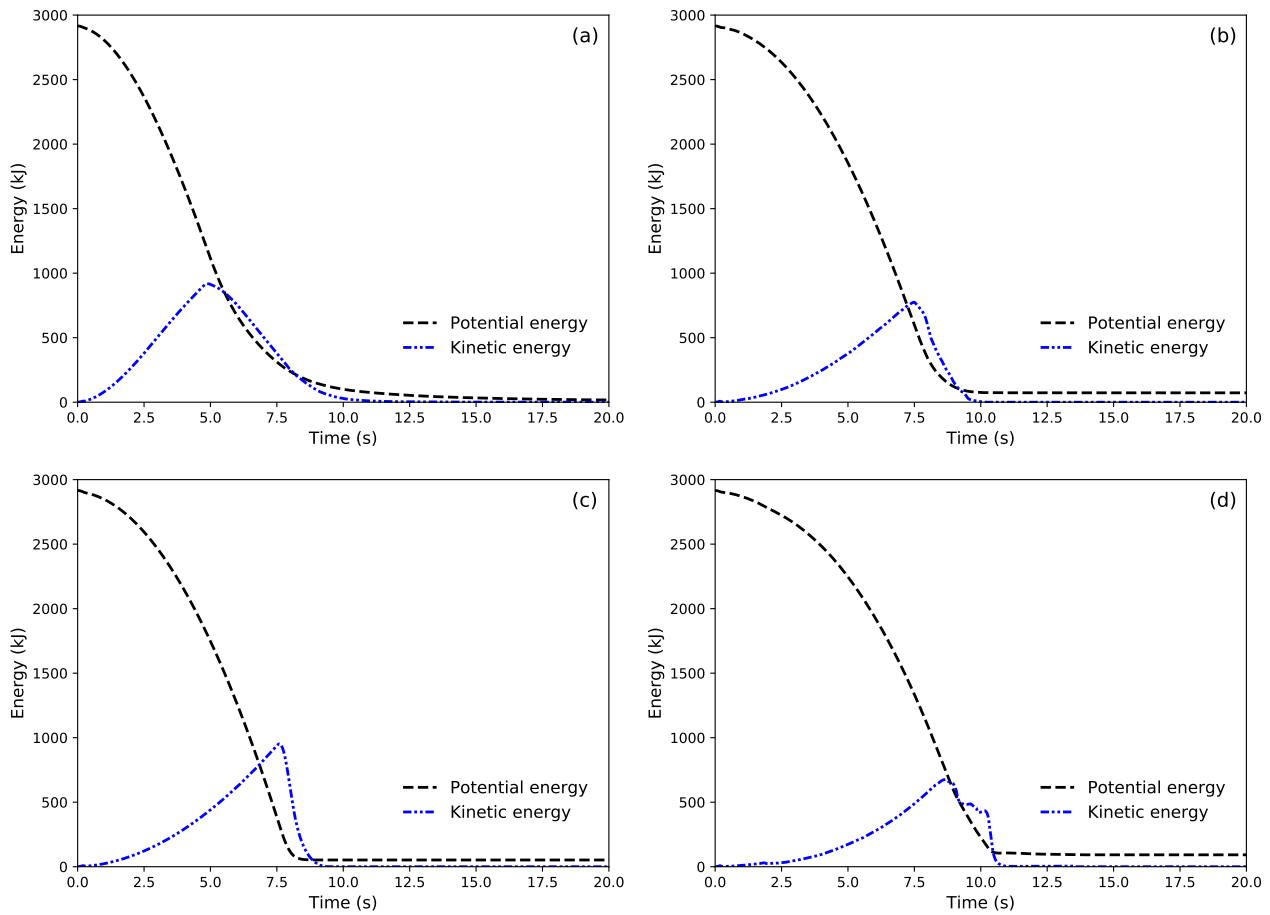
Figure A1. Evolution of potential and kinetic energy of the flows in the four typical flow regimes. (a) cold dense; (b) warm shear; (c) warm plug; (d) sliding slab.

The energy dissipation is contributed from 1) internal force of the material and 2) external force on the material from the boundary/slope. As illustrated in Fig. A3, in all the four cases, the dissipated energy from the boundary is much higher than that dissipated inside the material. This is consistent with the results in Gracia et al. (2019).

470
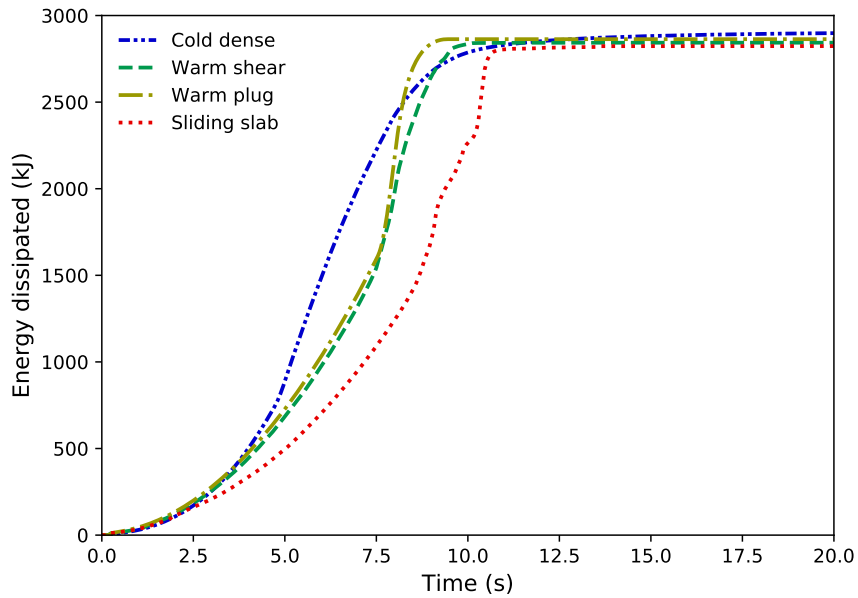
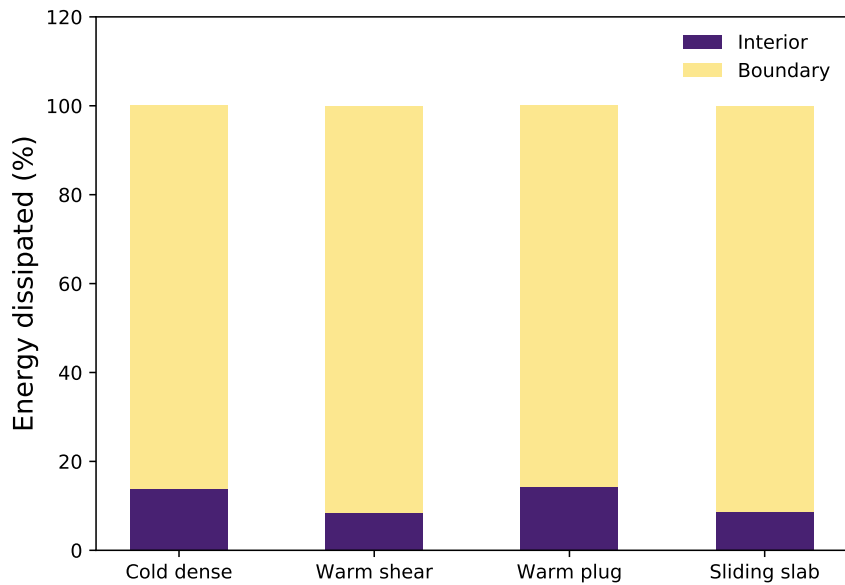**Figure A2.** Evolution of dissipated energy of the flows in the four typical flow regimes.

Figure A3. Energy dissipation inside the flow and through the boundary bed in the flows with the different flow regimes.

475 *Author contributions.* J.G. designed the study and obtained the funding. X.L. conducted the study, performed the simulations and wrote the paper under the supervision of J.G.. B.S. commented on the paper and provided guidance on the flow regime transitions. C.J. developed the MPM tool, which has been used in this study.

Competing interests. The authors declare that they have no conflict of interests.

References

480

Abdelrazek, A. M., Kimura, I., and Shimizu, Y.: Numerical simulation of a small-scale snow avalanche tests using non-Newtonian SPH model, Journal of Japan Society of Civil Engineers, 70, I_681–I_690, 2014.

Abe, K. and Konagai, K.: Numerical simulation for runout process of debris flow using depth-averaged material point method, Soils and Foundations, 56, 869–888, 2016.

485 Ancey, C.: Snow avalanches, in: Oxford Research Encyclopedia of Natural Hazard Science, 2016.

Barbolini, M., Gruber, U., Keylock, C., Naaim, M., and Savi, F.: Application of statistical and hydraulic-continuum dense-snow avalanche models to five real European sites, Cold Regions Science and Technology, 31, 133–149, 2000.

Chandel, C., Srivastava, P. K., and Mahajan, P.: Determination of failure envelope for faceted snow through numerical simulations, Cold Regions Science and Technology, 116, 56–64, 2015.

490 Choubin, B., Borji, M., Mosavi, A., Sajedi-Hosseini, F., Singh, V. P., and Shamshirband, S.: Snow avalanche hazard prediction using machine learning methods, Journal of Hydrology, 577, 123 929, 2019.

Christen, M., Kowalski, J., and Bartelt, P.: RAMMS: Numerical simulation of dense snow avalanches in three-dimensional terrain, Cold Regions Science and Technology, 63, 1–14, 2010.

Delparte, D., Jamieson, B., and Waters, N.: Statistical runout modeling of snow avalanches using GIS in Glacier National Park, Canada, Cold
495 Regions Science and Technology, 54, 183–192, 2008.

Eglit, M., Yakubenko, A., and Zayko, J.: A review of Russian snow avalanche models—From analytical solutions to novel 3D models, Geosciences, 10, 77, 2020.

Faug, T., Turnbull, B., and Gauer, P.: Looking beyond the powder/dense flow avalanche dichotomy, Journal of Geophysical Research: Earth Surface, 123, 1183–1186, 2018.

500 Fischer, J.-T., Kowalski, J., and Pudasaini, S. P.: Topographic curvature effects in applied avalanche modeling, Cold Regions Science and Technology, 74, 21–30, 2012.

Fischer, J.-T., Fromm, R., Gauer, P., and Sovilla, B.: Evaluation of probabilistic snow avalanche simulation ensembles with Doppler radar observations, Cold regions science and technology, 97, 151–158, 2014.

Fischer, J.-T., Kofler, A., Fellin, W., Granig, M., and Kleemayr, K.: Multivariate parameter optimization for computational snow avalanche
505 simulation, Journal of Glaciology, 61, 875–888, 2015.

Gauer, P.: Comparison of avalanche front velocity measurements and implications for avalanche models, Cold Regions Science and Technology, 97, 132–150, 2014.

Gauer, P., Issler, D., Lied, K., Kristensen, K., and Sandersen, F.: On snow avalanche flow regimes: Inferences from observations and measurements, in: Proceedings Whistler 2008 International Snow Science Workshop September 21-27, 2008, p. 717, 2008.

510 Gaume, J.: Prédétermination des hauteurs de départ d'avalanches. Modélisation combinée statistique-mécanique, Ph.D. thesis, Grenoble, 2012.

Gaume, J., Chambon, G., and Naaim, M.: Quasistatic to inertial transition in granular materials and the role of fluctuations, Physical Review E, 84, 051 304, 2011.

Gaume, J., Gast, T., Teran, J., van Herwijnen, A., and Jiang, C.: Dynamic anticrack propagation in snow, Nature Communications, 9, 1–10,
515 2018a.

Gaume, J., Gast, T., Teran, J., van Herwijnen, A., and Jiang, C.: Unified modeling of the release and flow of snow avalanches using the material point method, in: Geophysical Research Abstracts, vol. 20, 2018b.

Gaume, J., van Herwijnen, A., Gast, T., Teran, J., and Jiang, C.: Investigating the release and flow of snow avalanches at the slope-scale using a unified model based on the material point method, Cold Regions Science and Technology, 168, 102 847, 2019.

520 Gracia, F., Villard, P., and Richefeu, V.: Comparison of two numerical approaches (DEM and MPM) applied to unsteady flow, Computational Particle Mechanics, 6, 591–609, 2019.

Gubler, H., Hiller, M., Klausegger, G., and Suter, U.: Messungen an Fliesslawinen. Zwischenbericht, in: Internal Report 41, Swiss Federal Institute for Snow and Avalanche Research, 1986.

Hagenmuller, P., Chambon, G., and Naaim, M.: Microstructure-based modeling of snow mechanics: a discrete element approach, Cryosphere,
525 9, 1969–1982, 2015.

Issler, D. and Pérez, M. P.: Interplay of entrainment and rheology in snow avalanches: a numerical study, Annals of Glaciology, 52, 143–147, 2011.

Jiang, C., Schroeder, C., Selle, A., Teran, J., and Stomakhin, A.: The affine particle-in-cell method, ACM Transactions on Graphics (TOG), 34, 1–10, 2015.

530 Jiang, C., Schroeder, C., Teran, J., Stomakhin, A., and Selle, A.: The material point method for simulating continuum materials, in: ACM SIGGRAPH 2016 Courses, pp. 1–52, 2016.

Kern, M., Bartelt, P., Sovilla, B., and Buser, O.: Measured shear rates in large dry and wet snow avalanches, Journal of Glaciology, 55, 327–338, 2009.

Keshari, A. K., Satapathy, D. P., and Kumar, A.: The influence of vertical density and velocity distributions on snow avalanche runout, Annals
535 of Glaciology, 51, 200–206, 2010.

Klár, G., Gast, T., Pradhana, A., Fu, C., Schroeder, C., Jiang, C., and Teran, J.: Drucker-prager elastoplasticity for sand animation, ACM Transactions on Graphics (TOG), 35, 1–12, 2016.

Köhler, A., McElwaine, J., and Sovilla, B.: GEODAR Data and the flow regimes of snow avalanches, Journal of Geophysical Research: Earth Surface, 123, 1272–1294, 2018.

540 Larsson, S., Prieto, J. M. R., Gustafsson, G., Häggblad, H.-Å., and Jonsén, P.: The particle finite element method for transient granular material flow: modelling and validation, Computational Particle Mechanics, pp. 1–21, 2020.

Lied, K. and Bakkehøi, K.: Empirical calculations of snow–avalanche run–out distance based on topographic parameters, Journal of Glaciology, 26, 165–177, 1980.

Mast, C. M., Arduino, P., Miller, G. R., and Mackenzie-Helnwein, P.: Avalanche and landslide simulation using the material point method:
545 flow dynamics and force interaction with structures, Computational Geosciences, 18, 817–830, 2014.

McClung, D. and Gauer, P.: Maximum frontal speeds, alpha angles and deposit volumes of flowing snow avalanches, Cold Regions Science and Technology, 153, 78–85, 2018.

Naaim, M., Naaim-Bouvet, F., Faug, T., and Bouchet, A.: Dense snow avalanche modeling: flow, erosion, deposition and obstacle effects, Cold Regions Science and Technology, 39, 193–204, 2004.

550 Naaim, M., Durand, Y., Eckert, N., and Chambon, G.: Dense avalanche friction coefficients: influence of physical properties of snow, Journal of Glaciology, 59, 771–782, 2013.

Papakrivopoulos, V.: Development and preliminary evaluation of the main features of the Particle Finite Element Method (PFEM) for solid mechanics, Master's thesis, Delft University of Technology, 2018.

Rammer, L., Kern, M., Gruber, U., and Tiefenbacher, F.: Comparison of avalanche-velocity measurements by means of pulsed Doppler radar, continuous wave radar and optical methods, Cold Regions Science and Technology, 50, 35–54, 2007.

Rauter, M. and Köhler, A.: Constraints on Entrainment and Deposition Models in Avalanche Simulations from High-Resolution Radar Data, Geosciences, 10, 9, 2020.

Rauter, M., Kofler, A., Huber, A., and Fellin, W.: faSavageHutterFOAM 1.0: depth-integrated simulation of dense snow avalanches on natural terrain with OpenFOAM, Geoscientific Model Development, 11, 2923–2939, 2018.

Raymond, S. J., Jones, B., and Williams, J. R.: A strategy to couple the material point method (MPM) and smoothed particle hydrodynamics (SPH) computational techniques, Computational Particle Mechanics, 5, 49–58, 2018.

Reiweger, I., Gaume, J., and Schweizer, J.: A new mixed-mode failure criterion for weak snowpack layers, Geophysical Research Letters, 42, 1427–1432, 2015.

Salazar, F., Irazábal, J., Larese, A., and Oñate, E.: Numerical modelling of landslide-generated waves with the particle finite element method (PFEM) and a non-Newtonian flow model, International Journal for Numerical and Analytical Methods in Geomechanics, 40, 809–826, 2016.

Scapozza, C.: Entwicklung eines dichte-und temperaturabhängigen Stoffgesetzes zur Beschreibung des visko-elastischen Verhaltens von Schnee, Ph.D. thesis, ETH Zürich, 2004.

Simo, J. and Meschke, G.: A new class of algorithms for classical plasticity extended to finite strains. Application to geomaterials, Computational Mechanics, 11, 253–278, 1993.

Simo, J. C.: Algorithms for static and dynamic multiplicative plasticity that preserve the classical return mapping schemes of the infinitesimal theory, Computer Methods in Applied Mechanics and Engineering, 99, 61–112, 1992.

Soga, K., Alonso, E., Yerro, A., Kumar, K., and Bandara, S.: Trends in large-deformation analysis of landslide mass movements with particular emphasis on the material point method, Géotechnique, 66, 248–273, 2016.

Sovilla, B. and Bartelt, P.: Observations and modelling of snow avalanche entrainment, Natural Hazards and Earth System Sciences, 2, 169–179, 2002.

Sovilla, B., Burlando, P., and Bartelt, P.: Field experiments and numerical modeling of mass entrainment in snow avalanches, Journal of Geophysical Research: Earth Surface, 111, 2006.

Sovilla, B., Margreth, S., and Bartelt, P.: On snow entrainment in avalanche dynamics calculations, Cold Regions Science and Technology, 47, 69–79, 2007.

Sovilla, B., McElwaine, J. N., Schaer, M., and Vallet, J.: Variation of deposition depth with slope angle in snow avalanches: Measurements from Vallée de la Sionne, Journal of Geophysical Research: Earth Surface, 115, 2010.

Sovilla, B., McElwaine, J. N., and Louge, M. Y.: The structure of powder snow avalanches, Comptes Rendus Physique, 16, 97–104, 2015.

Srivastava, P., Chandel, C., and Mahajan, P.: Micromechanical modeling of elastic and strength properties of snow, SLAM3-Slab Avalanche Multiscale Mechanical Modeling, pp. 3–5, 2017.

Steinkogler, W., Sovilla, B., and Lehning, M.: Influence of snow cover properties on avalanche dynamics, Cold Regions Science and Technology, 97, 121–131, 2014.

Stomakhin, A., Schroeder, C., Chai, L., Teran, J., and Selle, A.: A material point method for snow simulation, ACM Transactions on Graphics, 32, 1–10, 2013.

Techel, F., Jarry, F., Kronthaler, G., Mitterer, S., Nairz, P., Pavšek, M., Valt, M., and Darms, G.: Avalanche fatalities in the European Alps: long-term trends and statistics, Geographica Helvetica, 71, 147–159, 2016.

Zabala, F. and Alonso, E.: Progressive failure of Aznalcóllar dam using the material point method, Géotechnique, 61, 795–808, 2011.